JASA ARTICLE

Extension of Amiet's theory to circular geometry

Rui Pedro Gonçalves,[1,2,a] Andrea P. C. Bresciani,[1] and Christophe Schram[1]
[1]*von Karman Institute for Fluid Dynamics, 72 chaussée de Waterloo, St-Genesius-Rode, 1640, Belgium*
[2]*University of Twente, PO Box 217, Enschede, 7500 AE, The Netherlands*

ABSTRACT:
This paper proposes and presents derivations of two analytical methods based on Amiet's theory to predict the aerodynamic broadband noise of a thin annulus. The first approach extends the thin annulus model proposed by Roger [(2010). J. Fluid Mech. **653**, 337–364] for leading-edge noise to trailing-edge noise by adapting Amiet's theory to a circular geometry. The second approach, referred to as the segmentation model, subdivides the annulus into noise-emitting flat plates, which are addressed with classical Amiet's theory. The results for the leading-edge thin annulus model matched well with the previously established results and experimental data. For the trailing-edge noise model, no reference results or experiments were available for direct comparison. The trailing-edge segmentation model showed good agreement with the thin annulus model, proving to be a valid method for trailing-edge noise prediction. Regarding the leading-edge segmentation model, an offset was observed, resulting in a consistent underprediction compared to the thin annulus model. Additional considerations were given about the ring's geometrical characteristics and their impact on the analytical model and noise predictions. These models provide a cost-effective approach, as the inputs can be derived from Reynolds-averaged Navier–Stokes simulations, making them suitable for numerous engineering applications, including ducted turbines, propellers, and other aerodynamic systems.
 https://doi.org/10.1121/10.0039542
(Received 1 March 2025; revised 16 September 2025; accepted 19 September 2025; published online 21 October 2025)
[Editor: Didier Dragna] Pages: 3133–3151

I. INTRODUCTION

The interaction of turbulence with the leading-edge (LE) and trailing-edge (TE) of a hollow cylindrical shape, axially aligned with the flow, produces broadband noise. This geometry is of significant research interest due to its prevalence in many aerodynamic applications where noise emissions are relevant. For example, in diffuser-augmented wind turbines, computations with lattice Boltzmann method have shown that, under low turbulence intensity, the diffuser TE is the primary noise source in most directions, exceeding the rotor's contributions (Freire-Guimaraes *et al.*, 2022). This effect results from the rotor-induced acceleration of flow along the suction side in the azimuthal direction, which triggers the transition to fully turbulent flow and increases the thickness of the boundary layer, leading to the increase in TE broadband noise. Given the similarity in flow conditions and geometry, a comparable effect may be anticipated in other applications, such as ducted propulsors in aviation (Bridges *et al.*, 2001) and ducted fans (Ahmed *et al.*, 2024) or ducted propellers (Malgoezar *et al.*, 2019). Another field of application is the noise associated with nozzle flows, where the TE noise of nozzle lips dominates over the jet noise at low Mach numbers (Henderson *et al.*, 2004; Olsen *et al.*, 1973; Olsen and Karchmer, 1976; Williams and Gordon, 1965). While TE and LE noise associated with the flow over an airfoil has been extensively analyzed numerically and experimentally since the early 1970s (Ffowcs Williams and Hall, 1970; Amiet, 1975, 1976; Howe, 1978; Brooks and Hodgson, 1981; Brooks *et al.*, 1989; Howe, 1999), few measurements have been reported on the noise generated by hollow cylindrical shapes (Roger, 2010; Ahmed *et al.*, 2024; Olsen *et al.*, 1973; Olsen and Karchmer, 1976) and even less attempts have been made in trying to predict the TE or LE noise radiated (Roger, 2010; Freire-Guimaraes *et al.*, 2022). This work addresses this gap focusing on the prediction of LE and TE broadband noise using analytical models.

An analytical model for predicting broadband noise generated by the interaction of flow turbulence with an infinitely thin flat plate aligned with the flow velocity was proposed by Amiet (1975, 1976). It provides a framework to compute both LE and TE broadband noise in the far-field. Back-scattering corrections to the aeroacoustic transfer function have been developed to account for effects due to the finite chord length (Roger and Moreau, 2005; Bresciani *et al.*, 2022). Thanks to its wide applicability, Amiet's theory is effectively used for predicting airfoil noise of helicopter rotors (Schlinker and Amiet, 1981), fans (Roger and Moreau, 2004), wind turbines (Tian and Cotté, 2016), and aircraft propellers (Blandeau and Joseph, 2011).

Roger (2010) extended Amiet's flat plate theory to an equivalent circular geometry, providing the expression to compute the LE impingement noise of an infinitely thin annulus, further also referred to as a ring, with a sufficiently small chord-to-radius ratio such that duct modal behavior and multiple reflections between diametrically opposite walls can be disregarded. The model was developed to validate Amiet's theory by addressing the limitations of rectangular airfoil setups (Roger and Moreau, 2010), such as spurious noise sources

[a]Email: rui.goncalves@vki.ac.be

from side plates and limited validation off the mid-span plane, through the use of a circular geometry that allows for axisymmetric noise radiation and reduces the amount of scattering effects. However, a TE noise model for a circular geometry has not been proposed. Such a model is particularly important in applications like ducted propellers and wind turbines, where the duct TE noise can dominate the overall noise emissions due to the reduced impact of LE noise. Indeed, the increased thickness and LE radius of an airfoil significantly reduce LE noise, with thickness contributing more at mid frequencies and LE radius at higher frequencies (Devenport *et al.*, 2010; Botero-Bolívar *et al.*, 2023). This thickness-dependent reduction in LE noise emphasizes the relative importance of TE noise in diffuser and duct-shaped configurations. Furthermore, a model for TE noise emitted by circular geometries would provide insight into involved physics of the noise radiated by nozzle lips despite necessary simplifications, such as assuming a semi-infinite cylinder due to the absence of a back-scattering edge, and neglecting the velocity mismatch between the inner and outer sides of the nozzle. This paper addresses both the LE and TE noise of circular geometries using two approaches. The first approach, called the thin annulus model, extends Amiet's theory for TE noise to circular shapes, following the methodology of Roger (2010). The second approach, referred to as the segmentation approach, describes the ring as a discrete sum of flat plates using classical Amiet theory. Once validated, the segmentation approach can be applied to non-circular geometries, widening its applicability to a broader range of engineering problems.

To address this gap, we implement the LE formulation from Roger (2010) and compare it with the analytical and experimental results published in the same article. This comparison allows us to indirectly validate the TE derivation and implementation proposed in this work, as they follow a similar approach. The TE noise formulation, which is the original contribution of this work, is derived in parallel to the LE noise model following the same approach as the reference paper. Further confidence in the correctness of our result is brought by comparing the results of our segmentation approach with the ring model.

The paper is organized as follows: Sec. II describes the two analytical methodologies, the comparison and validation are discussed in Sec. III, and the conclusions are discussed in Sec. IV. Finally, Appendix A provides an extended derivation of the segmentation approach, addressing the reference frame transformations involved, while Appendix B demonstrates that the ring's aeroacoustic transfer function is identical to that of the flat plate.

II. METHODS

Section II A reviews Amiet's theory for rectangular flat plates and introduces the notation. In Sec. II B, we derive the thin annulus model for both LE and TE noise. Finally, Sec. II C presents the segmentation approach.

A. Review of Amiet's theory for flat plates

The power spectral density (PSD) of the acoustic pressure generated by a fluctuating hydrodynamic wall-pressure field moving with the mean flow on a surface $S(\mathbf{y})$, is determined using dipole sources. These dipole sources have strengths equivalent to the forces on the surface. Given the random nature of turbulence, the loading is described statistically using the cross-PSD of the wall-pressure jump between two points, $S_{ll}, (\mathbf{y}, \mathbf{y}', \omega)$. The cross-PSD of the loading can then be used to compute the PSD of the acoustic pressure, S_{pp}, at the observer position $\mathbf{x} = (x_1, x_2, x_3)$ in the acoustic far-field and angular frequency ω through (Bresciani, 2024)

$$S_{pp}(\mathbf{x}, \omega) = \int_{S(\mathbf{y})} \int_{S(\mathbf{y}')} \left(\frac{\omega\, x_3}{4\pi\, c_0} \right)^2 \frac{S_{ll}\,(\mathbf{y}, \mathbf{y}', \omega)}{\sigma_s^2 \sigma'_{s2}} \times e^{-i\omega(\sigma - \sigma')/c_0}\, \mathrm{d}S(\mathbf{y})\, \mathrm{d}S(\mathbf{y}'), \tag{1}$$

where $k = \omega/c_0$ is the acoustic wavenumber, $\sigma_s = \sqrt{(x_1 - y_1)^2 + \beta^2 (x_2 - y_2)^2 + \beta^2 x_3^2}$ denotes the distance from the airfoil to the listener corrected for the convection effects with $\beta^2 = 1 - M^2$ and $\sigma = [\sigma_s - M(x_1 - y_1)]/\beta^2$. Finally, $M = U/c_0$ denotes the Mach number based on the freestream velocity U and speed of sound c_0.

Based on Eq. (1), Amiet (1975, 1976) proposed the rectangular thin plate theory, applicable to the LE noise and TE noise generated by airfoils. The foundation of the aerodynamic interaction is based on linearized airfoil theory and the application of Schwartzchild's theorem (Amiet, 1975; Roger and Moreau, 2005), with the acoustic radiation based on Curle's acoustic analogy (Amiet, 1975). In these semi-analytical models, the lift generated by the unsteady wall pressure fields is the equivalent source of noise. Said pressure fields are induced by the advection of turbulent structures, which differ for leading and TE cases. This results in different lift fluctuations for LE and TE noise, leading to separate expressions for LE and TE broadband PSD at the observer position. As a convention, the coordinate axes for the LE and TE cases have the same orientation but are centered differently: at the mid-chord of the airfoil for the LE case and at the TE for the TE case (see Fig. 1).

The approximations of the sound pressure PSD for an observer in the acoustic and geometric far-field, i.e., $\sigma_s \approx S_0 = \sqrt{x_1^2 + \beta^2 (x_2^2 + x_3^2)}$, read

$$S_{pp}^{LE}(\mathbf{x}, \omega) = \left(\frac{\omega\, x_3\, c\, \rho_0}{2\, c_0\, S_0^2} \right)^2 \frac{L}{2} U \pi\, |\mathcal{L}^{LE}(x_1, K_1, K_2)|^2 \times \Phi_{ww}(K_1, K_2), \tag{2}$$

for LE noise, and

$$S_{pp}^{TE}(\mathbf{x}, \omega) = \left(\frac{\omega\, x_3\, c}{4\pi\, c_0\, S_0^2} \right)^2 \frac{L}{2}\, |\mathcal{L}^{TE}(x_1, K_1, K_2)|^2 \times l_y(\omega, K_2)\, \Phi_{pp}(\omega) \tag{3}$$

https://doi.org/10.1121/10.0039542

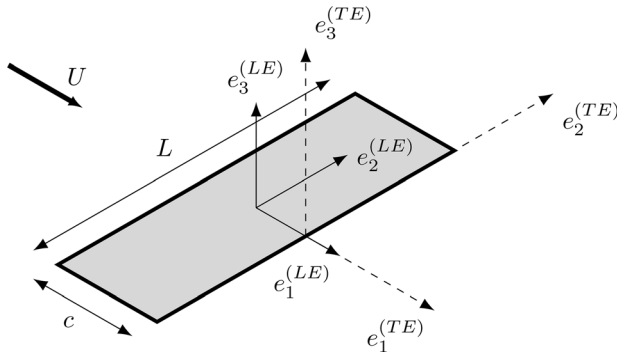

FIG. 1. Frame of reference used in Amiet theory for LE (—) or TE (- -) noise prediction.

for TE noise. In Eqs. (2) and (3), c and L are the chord and span, respectively, ρ and c_0 are the density and speed of sound in air, $K_1 = \omega/U$ is the streamwise aerodynamical wavenumber, and $K_2 = k\,x_2/S_0$ are the spanwise wavenumbers; the aeroacoustic transfer functions, $\mathcal{L}^{LE}$ and $\mathcal{L}^{TE}$, describe the relation between the surface pressure jump (for TE noise) or the upwash velocity perturbation (for LE noise). In this work, the formulation proposed by Bresciani *et al.* (2022) is used. The spectra Φ_{ww} and Φ_{pp} represent the two-dimensional power spectral densities for the LE and TE case, and the spanwise coherence length l_y is defined as (Bresciani, 2024)

$$l_y(\omega, k_2) = \frac{1}{S_{qq}(\omega, 0)} \int_0^{+\infty} S_{qq}(\omega, y_2) \mathrm{e}^{-\mathrm{i}k_2 y_2} \mathrm{d}y_2, \tag{4}$$

where $S_{qq}(\omega, 0) = \Phi(\omega)$ is the surface pressure spectrum observed in the middle plane.

The expressions for LE and TE noise present a similar structure. The primary difference lies in the two-dimensional spectra characterizing the load. For the LE case, Φ_{ww} is the incoming turbulence spectrum. For the TE case, Φ_{pp} is the point spectral density of the pressure field at the TE. The computational approach for these spectra is elaborated in Sec. II D. The transfer functions differ between the LE and TE cases due to the differences in the airfoil response to the perturbations [see Amiet (1975) for LE noise and Amiet (1976) for TE noise].

B. Thin annulus model

Roger (2010) extended the flat plate Amiet's theory to the broadband noise radiated by the LE of a thin annulus. This model adapts classical Amiet's principles to a hollow cylindrical surface $S(y)$. In this work, we propose the TE noise theory following the same approach. The adaptation considers similar assumptions, such as thin circular geometry under aligned freestream velocity U, with radius r_0 and chord length c, ensuring axial symmetry in the coordinate system, as represented in Fig. 2. The observer's position is denoted by $\mathbf{x} = (x_1, x_2, x_3)$, and the source is defined by $\mathbf{y} = (y_1, r_0\theta)$ in the e_1, s reference frame, where s is the curvilinear coordinate following the circumference of the annulus. The source position can be equivalently expressed as $\mathbf{y} = (y_1, y_2, y_3)$ in the $\mathbf{e} = (e_1, e_2, e_3)$ frame of reference. The origin is centered with the ring, at mid-chord. The relative position vector between the observer and the source is denoted by $\mathbf{R} = \mathbf{x} - \mathbf{y}$, and the projected distance T represents the projection of $\mathbf{R}$ onto the frontal plane defined by coordinates e_2 and e_3.

The acoustic PSD at the receiver position $\mathbf{x}$ is obtained applying the expected value operator to the product of the acoustic pressure $\tilde{p}$ and its complex conjugate, $\tilde{p}^*$ (Amiet, 1975),

$$S_{pp}(\mathbf{x}, \omega) = \lim_{T_\infty \to +\infty} \left\{ \frac{\pi}{T_\infty} \mathrm{E}[\tilde{p}(\mathbf{x}, \omega)\, \tilde{p}^*(\mathbf{x}, \omega)\,] \right\}, \tag{5}$$

where the symbol $\tilde{}$ denotes the Fourier transform. The integration time T_∞ represents the averaging interval over which the turbulent structures pass over the airfoil (Amiet, 1975). The stochastic contribution of the point dipole dF to the acoustic pressure is defined by the expression

$$\mathrm{d}p'(\mathbf{x}, t) = \frac{R_2 \sin\theta + R_3 \cos\theta}{4\pi c_0 S_0^2} \cdot \left[\frac{\partial(\mathrm{d}F)}{\partial t'} \right]_{t - \frac{R_t}{c_0}}, \tag{6}$$

where the loading $\mathrm{d}F = l(y_1, \theta, t)\, n\mathrm{d}S$ denotes the unsteady lift force per unit area with n being its normal component, $R_t = (R_s - M(x_1 - y_1))/\beta^2$ is the modified distance, and S_0 is the far-field corrected distance with $S_0^2 = x_1^2 + \beta^2(x_2^2 + x_3^2)$.

The point dipole contribution to acoustic pressure is expressed in Fourier form, as

$$\tilde{p}(\mathbf{x}, \omega) = \frac{-\mathrm{i}\omega}{4\pi c_0 S_0^2} \int_0^{2\pi} \int_{-c/2}^{c/2} (x_2 \sin\theta + x_3 \cos\theta) \times \tilde{l}(y_1, \theta, \omega)\, \mathrm{e}^{\mathrm{i}kR_T}\, r_0\, \mathrm{d}y_1 \mathrm{d}\theta. \tag{7}$$

Substituting Eq. (7) into Eq. (5) by multiplying $\tilde{p}$ with its complex conjugate $\tilde{p}^*$, we obtain

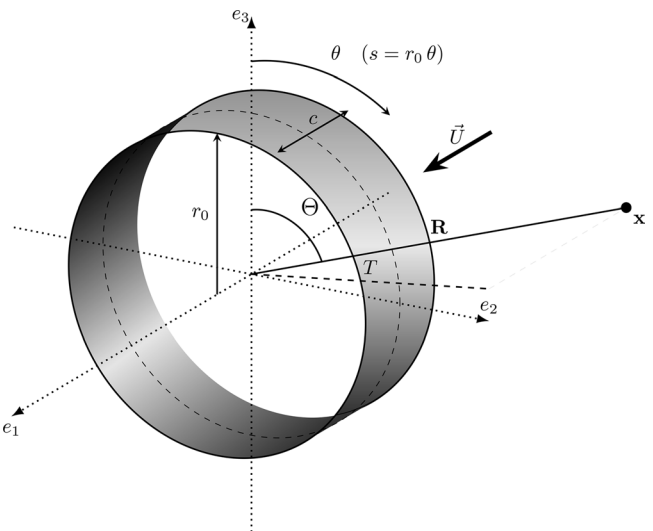

FIG. 2. Frame of reference used for ring LE noise calculation.

$$S_{pp}(\mathbf{x},\omega) = \left(\frac{-\mathrm{i}\omega}{4\pi c_0 S_0^2}\right)^2 \int\!\!\int_0^{2\pi} \int\!\!\int_{-c/2}^{c/2} (x_2\sin\theta + x_3\cos\theta) \times (x_2\sin\theta' + x_3\cos\theta')\, S_{ll}(y_1, y_1', \theta, \theta', \omega) \times \mathrm{e}^{\mathrm{i}k(R_T - R_T')}\, r_0^2\, \mathrm{d}y_1 \mathrm{d}y_1' \mathrm{d}\theta \mathrm{d}\theta', \tag{8}$$

where $S_{ll}(y_1, y_1', \theta, \theta', \omega) = \tilde{l}(y_1, \theta, \omega)\, \tilde{l}^*(y_1', \theta', \omega)$ is the cross-spectral power density of the unsteady lift, expressed as

$$S_{ll}(y_1, y_1', \theta, \theta', \omega) = \lim_{T_\infty \to +\infty} \left\{ \frac{\pi}{T_\infty} \mathrm{E}\left[\tilde{l}(y_1, \theta, \omega)\, \tilde{l}^*(y_1', \theta', \omega)\right] \right\}. \tag{9}$$

The unsteady lift $\tilde{l}(y_1, \theta, \omega)$ is a function of the pulsation ω and position on the annulus surface (y_1, θ). The function takes different forms for the LE and TE cases, i.e.,

$$\tilde{l}(y_1, \theta, \omega) = \begin{cases} 2\pi\rho_0 \displaystyle\sum_{n=-\infty}^{\infty} \tilde{w}_n(K_1)\, g(y_1, K_1, k_n)\, \mathrm{e}^{\mathrm{i}n\theta} & \text{(LE)}, \\ \dfrac{1}{U_c} \displaystyle\sum_{n=-\infty}^{\infty} \tilde{q}_n(K_1) f(y_1, K_1, k_n)\, \mathrm{e}^{\mathrm{i}n\theta} & \text{(TE)}, \end{cases} \tag{10}$$

where U_c is the convective velocity, $k_n = n/r_0 = n\,\theta/s$ is the azimuthal wavenumber of the gust of mode n and $s = r_0\,\theta$ is the curvilinear coordinate, $\tilde{w}_n$ and $\tilde{q}_n$ represent the Fourier transforms of the incident perturbations at the LE and TE, and finally, $g(y_1, K_1, k_n)$ and $f(y_1, K_1, k_n)$ are the ring's response functions to the LE and TE perturbation, respectively. Consequently, we obtain

$$S_{ll}(y_1, y_1', \theta, \theta', \omega) = \begin{cases} (2\pi\rho_0)^2 \displaystyle\sum_{n=-\infty}^{\infty} \tilde{w}_n(K_1)\, \tilde{w}_m^*(K_1)\, g(y_1, K_1, k_n)\, g^*(y_1', K_1, k_n)\, \mathrm{e}^{\mathrm{i}n(\theta-\theta')} & \text{(LE)}, \\ \left(\dfrac{1}{U_c}\right)^2 \displaystyle\sum_{n=-\infty}^{\infty} \tilde{q}_n(K_1)\, \tilde{q}_m^*(K_1) f(y_1, K_1, k_n) f^*(y_1', K_1, k_n)\, \mathrm{e}^{\mathrm{i}n(\theta-\theta')} & \text{(TE)}. \end{cases}$$

Considering the stochastic orthogonality of the incoming gusts, the expected value operator is again applied to the product of the random quantities, providing

$$\lim_{T_\infty \to +\infty} \left\{ \frac{\pi}{T_\infty} \mathrm{E}\left[\tilde{w}_n(K_1)\tilde{w}_m^*(K_1)\right] \right\} = 2\pi \frac{U}{r_0}\, \delta(n-m)\, \Phi_{ww}(K_1, k_n),$$

$$\lim_{T_\infty \to +\infty} \left\{ \frac{\pi}{T_\infty} \mathrm{E}\left[\tilde{q}_n(K_1)\tilde{q}_m^*(K_1)\right] \right\} = 2\pi \frac{U_c}{r_0}\, \delta(n-m)\, \Phi_{qq}(K_1, k_n),$$

where δ is the Dirac delta function.

Using the previous definitions, we obtain $S_{ll}(y_1, y_1', \theta, \theta', \omega)$ for LE and TE cases

$$S_{ll} = \begin{cases} (2\pi\rho_0)^2\, 2\pi \dfrac{U}{r_0} \displaystyle\sum_{n=-\infty}^{\infty} \delta(n-m)\, \Phi_{ww}(K_1, k_n)\, g(y_1, K_1, k_n) g^*(y_1', K_1, k_n)\, \mathrm{e}^{\mathrm{i}n(\theta-\theta')} & \text{(LE)}, \\ \dfrac{2\pi}{U_c r_0} \displaystyle\sum_{n=-\infty}^{\infty} \delta(n-m)\, \Phi_{qq}(K_1, k_n) f(y_1, K_1, k_n) f^*(y_1', K_1, k_n)\, \mathrm{e}^{\mathrm{i}n(\theta-\theta')} & \text{(TE)}. \end{cases} \tag{13}$$

To obtain the expressions for S_{pp}, we replace S_{ll} from Eq. (13) into Eq. (8). Next, using the definition of R_T, we redefine the term $\mathrm{e}^{\mathrm{i}k(R_T - R_T')}$ in terms of y_1 and θ dependent components. Specifically, we introduce

$$R_T - R_T' = \frac{1}{\beta^2 S_0}\left[(x_1 - MS_0)(y_1' - y_1) + \beta^2 r_0 T \times (\cos(\theta' - \Theta) - \cos(\theta - \Theta))\right]. \tag{14}$$

We then separate the integrals by splitting the $\mathrm{d}y_1$ and $\mathrm{d}\theta$ terms. Following this, we highlight the conjugate terms. Finally, we perform a change of variable $y_1^* = 2(y_1/c)$ to nondimensionalize the integral. This allows to substitute $(x_2\sin\theta + x_3\cos\theta)$ with the equivalent projected coordinates $T\sin(\Theta)\sin(\theta) + T\cos(\Theta)\cos(\theta)$, which simplifies to $T\cos(\theta - \Theta)$. The following are the final expressions for the ring's LE and TE acoustic PSD in the far field

https://doi.org/10.1121/10.0039542

$$S_{pp}^{LE}(\mathbf{x},\omega) = \left(\frac{\omega\rho c}{4\,c_0 S_0^2}\right)^2 2\pi r_0 U \sum_{n=-\infty}^{\infty} \Phi_{ww}(K_1,k_n) \times |\mathcal{L}^{LE}(x_1,K_1,k_n)|^2 |\mathscr{J}|^2, \tag{15}$$

$$S_{pp}^{TE}(\mathbf{x},\omega) = \left(\frac{\omega c}{4\,c_0 S_0^2}\right)^2 \frac{\pi r_0}{2U_c} \sum_{n=-\infty}^{\infty} \Phi_{qq}(K_1,k_n) \times |\mathcal{L}^{TE}(x_1,K_1,k_n)|^2 |\mathscr{J}|^2, \tag{16}$$

with the surface pressure spectrum Φ_{qq} defined as

$$\Phi_{qq}(K_1,k_n) = \frac{U_c}{\pi}\, l_\theta(\omega,k_n)\, \Phi_{pp}(\omega), \tag{17}$$

where l_θ is the azimuthal correlation length, and Φ_{pp} is the local pressure spectral density. Equation (15) corresponds to the same expression found in Roger (2010), while Equation (16) is the original contribution of this work. The aeroacoustic transfer functions $\mathcal{L}$ are normalized by the chord and expressed as

$$\mathcal{L}(x_1,K_1,k_n) = \begin{cases} \displaystyle\int_{-1}^{1} g(y_1^*,K_1,k_n)\, e^{-\mathrm{i}y_1^* c/2k(x_1-MS_0)/\beta^2 S_0}\, \mathrm{d}y_1^* & \text{(LE)}, \\ \displaystyle\int_{-1}^{1} f(y_1^*,K_1,k_n)\, e^{-\mathrm{i}y_1^* c/2k(x_1-MS_0)/\beta^2 S_0}\, \mathrm{d}y_1^* & \text{(TE)}. \end{cases} \tag{18}$$

The expressions for the aeroacoustic transfer functions in Equation (18) are identical to those presented in Amiet (1975). In Appendix B, we demonstrate that these expressions lead to the same solution as the flat plate. Comprehensive solutions for $\mathcal{L}$ can be found in Roger and Moreau (2005) and Bresciani *et al.* (2022). Finally, the term $\mathscr{J}$ is defined as

$$\mathscr{J} = \mathrm{e}^{\mathrm{i}n\Theta} \int_0^{2\pi} T\cos(\theta-\Theta)\, \mathrm{e}^{-\mathrm{i}kr_0 T\cos(\theta-\Theta)/S_0} \mathrm{e}^{\mathrm{i}n(\theta-\Theta)} \mathrm{d}\theta, \tag{19}$$

and its absolute value squared was shown in Roger (2010) to be equivalent to

$$|\mathscr{J}|^2 = (2\pi)^2 T^2 \left(\mathrm{J}_n'\left(\frac{kr_0 T}{S_0}\right)\right)^2, \tag{20}$$

where J_n' is the derivative of the Bessel function of the first kind and $k = \omega/c_0$ is the acoustic wavenumber.

Equations (15) and (16) present some analogies with Eqs. (2) and (3). In both cases, the far-field acoustic PSD is related to the disturbance spectrum (Φ_{ww} and Φ_{qq} for the LE and TE noise cases, respectively) through an aeroacoustic transfer function. In the thin annulus theory, the transfer function $\mathcal{L}$ of the flat plate is modified by the function $\mathscr{J}$. Furthermore, spanwise wavenumber K_2 of the flat plate theory is replaced by the summation over the azimuthal wavenumbers k_n in the thin annulus theory. Even though there is a summation of modes n from $-\infty$ to ∞, as we will see later on, the modes close to $n = 0$ are more relevant, allowing us to shorten the range of n. As a result, this method provides increased efficiency over the integral computation of the segmentation approach. It is worth adding that due to the anti-symmetry $\mathrm{J}_n' = -\mathrm{J}_{-n}'$, it follows that $|\mathscr{J}(n)|^2 = |\mathscr{J}(-n)|^2$. This symmetry leads to the contribution of mode n and $-n$ being equal, allowing for further optimization.

As expected, the final expressions for the PSD [Eqs. (15) and (16)] do not depend on the angular position of the observer Θ, indicating the axisymmetry of the problem. As a consequence, the acoustic results computed at the meridional plane can be generalized to the three-dimensional space.

C. Segmentation approach

The segmentation approach consists in subdividing the ring into N flat plate segments, as illustrated in Fig. 3.

The circular shape's total broadband noise is obtained through the superposition of the separate N plates LE and TE noise, computed using Eqs. (2) and (3), resulting in

$$S_{pp}^{LE}(\mathbf{x},\omega) = \sum_{j=0}^{N} S_{pp,j}^{LE}(\mathbf{x},\omega),$$

$$S_{pp}^{TE}(\mathbf{x},\omega) = \sum_{j=0}^{N} S_{pp,j}^{TE}(\mathbf{x},\omega).$$

Taking into account for the terms constant for each segment j, we can develop the former expression to obtain the ring's S_{pp}^{LE} and S_{pp}^{TE},

$$S_{pp}^{LE}(\mathbf{x},\omega) = \left(\frac{\omega\rho c}{2c_0}\right)^2 \pi U \frac{L}{2} \sum_{j=0}^{N} \left(\frac{x_{3j}}{S_{0j}^2}\right)^2 \times |\mathcal{L}^{LE}(x_{1j},K_1,K_{2j})|^2\, \Phi_{ww}(K_1,K_{2j}), \tag{21}$$

$$S_{pp}^{TE}(\mathbf{x},\omega) = \left(\frac{\omega c}{4\pi c_0}\right)^2 \frac{L}{2} \sum_{j=0}^{N} \left(\frac{x_{3j}}{S_{0j}^2}\right)^2 |\mathcal{L}^{TE}(x_{1j}, K_1, K_{2j})|^2 \times \Phi_{pp}(\omega)\, l_y(\omega, K_{2j}), \quad (22)$$

where c is the ring chord, and the segment length L can be defined with the ring's radii r_0 and number of segments N as $L = 2r_0 \sin(\pi/N)$. The third component of the observer position x_{3j} and distance S_{0j}^2 are computed in the local reference frame of each segment j through the geometrical transformations detailed in Appendix A. For segment j, the observer relative positions and the corrected distance S_{0j} are obtained based on the observer-source relative position $\mathbf{R}$ with

$$x_{1j} = R_1 - l, \quad x_{2j} = R_2 \cos\theta_j - R_3 \sin\theta_j, \quad x_{3j} = R_2 \sin\theta_j + R_3 \cos\theta_j - r_0,$$

$$S_{0j} = \sqrt{x_{1j}^2 + \beta^2(x_{2j}^2 + x_{3j}^2)} = \sqrt{(R_1 - l)^2 + \beta^2\left(\left(R_2\cos\theta_j - R_3\sin\theta_j\right)^2 + \left(R_2\sin\theta_j + R_3\cos\theta_j - r_0\right)^2\right)},$$

where θ_j is the segment's azimuth and l adjusts the reference frame's axial position to match Amiet's theory, such that $l = 0$ for the LE case and $l = c/2$ for the TE case (see Fig. 1).

Differently from the thin annulus model, the segmentation model assumes independent, uncorrelated contributions from each segment, neglecting cross-correlations across the annulus. A methodology that incorporates cross correlation between segments would improve the model's accuracy and increase its consistency with the thin annulus model, which enforces coherence across the annulus through the azimuthal nodes.

D. Two-dimensional spectra and correlation length

The incoming turbulence spectrum Φ_{ww} can be obtained using the two-dimensional von Kármán turbulence spectrum model, given by

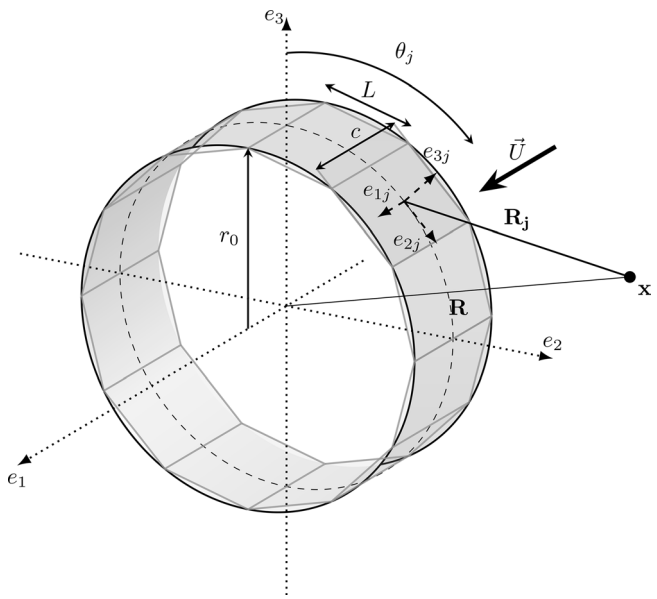

FIG. 3. Ring discretization and frame of reference used for segmentation approach.

$$\Phi_{ww}^{vK}(k_1,k_2) = \frac{4}{9\pi}\frac{u_{rms}^2}{k_e^2}\left(\frac{(k_1/k_e)^2 + (k_2/k_e)^2}{1 + (k_1/k_e)^2 + (k_2/k_e)^2}\right)^{7/3}, \quad (23)$$

where u_{rms} represents the root mean square velocity, and k_e is the wavenumber scale of the largest eddies, obtained as

$$k_e = \frac{\sqrt{\pi}}{\Lambda_f}\frac{\Gamma(5/6)}{\Gamma(1/3)},$$

where Λ_f denotes the characteristic length scale of the turbulence and Γ the gamma function. In the thin annulus model, k_n replaces k_2.

The frequency spectrum of the wall pressure fluctuations Φ_{pp} is obtained using semi-empirical wall pressure spectrum (WPS) models (Hwang *et al.*, 2009). Alternatively, the WPS can be obtained from experiments (dos Santos *et al.*, 2023; Salze *et al.*, 2014), TNO–Blake (Stalnov *et al.*, 2015) models or high-fidelity simulations, such as direct numerical simulations (Na and Moin, 1998; Pargal *et al.*, 2022; Pirozzoli and Bernardini, 2010) or large–eddy simulations (Wu and Piomelli, 2018; Cohen and Gloerfelt, 2018). There is a wide range of WPS models available, and the selection is based on the type of pressure gradient observed at the TE, as detailed in Gonçalves (2025). A zero-pressure gradient is expected for an infinitely thin annulus; therefore, Goody's model (Goody, 2004) is used in this work.

The inputs required for the WPS models are the parameters defining the turbulent boundary layer (BL) at the TE, i.e., the boundary layer thickness δ, the displacement thickness δ^*, the momentum thickness θ, the wall shear stress τ, and the edge velocity U_e. In the present work, these parameters are computed assuming that the boundary layer over the annulus can be approximated as the boundary layer of a flat plate. We expect this approximation to be valid for annuli with a radius much larger than the boundary layer thickness. In this case, the boundary layer thickness, displacement thickness, and momentum thickness are expressed as (White, 2009)

https://doi.org/10.1121/10.0039542

$$\frac{\delta}{c} = \frac{0.16}{\mathrm{Re}^{1/7}}, \quad \delta^* = \frac{1}{8}\delta, \quad \theta = \frac{7}{72}\delta, \tag{24}$$

where Re is the chord-based Reynolds number. The edge velocity U_e is calculated as $U_e = U_{[y=\delta]}$ (Griffin *et al.*, 2021). Finally, the wall shear stress τ is computed using Prandtl's one-seventh-power law (White, 2009; Prandtl, 1925), where the friction coefficient C_f is expressed as

$$C_f = \frac{0.027}{\mathrm{Re}^{1/7}}, \tag{25}$$

and $\tau = (1/2)\rho U^2 C_f$.

The azimuthal correlation length l_θ is also calculated using the same flat plate approximation. In this case, Corcos's model (Corcos, 1964) is widely employed in the literature [e.g., Roger and Moreau (2005); Moreau and Roger (2009)]. Formally, the azimuthal correlation length $l_\theta(\omega, k_n)$ is replaced by the spanwise correlation length $l_y(\omega, k_n)$ and calculated as (Corcos, 1964)

$$l_y(\omega, k_n) = \frac{1/L_2}{k_n^2 + (1/L_2)^2}, \tag{26}$$

where $L_2 = b_c U_c/\omega$ with $b_c = 1.47$ and $U_c = 0.7U$.

III. RESULTS AND DISCUSSION

The results obtained using the thin annulus model and the segmentation approach are compared in Sec. III B and in Sec. III C for LE noise and TE noise, respectively. In Sec. III A, the convergence of the segmentation approach and the ring model's sensitivity to input parameters is studied in Sec. III D.

A. Convergence study for the segmentation approach

To ensure accurate noise predictions using the segmentation approach, a convergence study was conducted to evaluate the impact of the number of segments N on the predicted noise levels and validate the robustness of the method.

When using Amiet's large aspect ration (AR) approximation, it is suggested to use airfoil segments with an $AR > 3$ [e.g., Tian (2016)]. The AR of N segments discretizing a ring is $AR = 2(r_0/c)\sin(\pi/N)$ and consequently, a larger number of segments N results in lower AR, potentially violating the large AR assumption. This limitation can be addressed using the arbitrary aspect ratio sine cardinal formulation. However, the significant computational cost due to the k_2 integration required for each segment might hamper some applications. Alternatively, an inverse strip approach can be used to predict the acoustic response of small airfoils by computing the difference between two larger airfoils whose spanwise lengths differ by that of the smaller airfoil (Christophe *et al.*, 2009; Kucukcoskun *et al.*, 2013). In this work, we mitigate this limitation by considering a ring with a large enough r_0/c ratio, increasing the AR of the individual segments.

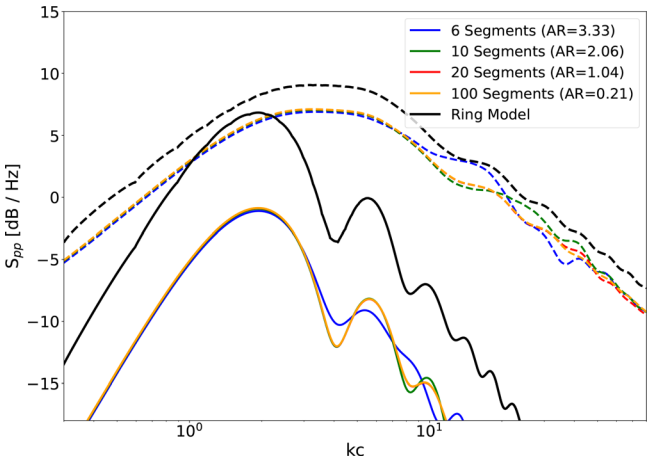

FIG. 4. LE (—) and TE (- -) convergence study of the number of segments N, compared to ring model using azimuthal modes ranging from $n = -400$ to $n = 400$ at a distance of $R = 26r_0$, and angular position of 120°. Turbulence intensity TI = 0.1%, integral length scale $\Lambda_f = 0.015$ m, and freestream velocity $U = 50$ m s^{-1}.

Figure 4 presents the LE and TE results of the convergence study carried on a ring under inflow $U = 50$ m s^{-1} with $r_0 = 1$ m and $c = 0.3$ m for an observer at a distance $R = 26r_0$ and angular position 120° (being 0° the upstream direction), showing the noise predictions for different number of segments. The results, valid for the LE and TE predictions, indicate that convergence is achieved with $N = 20$ segments, and increasing N beyond this value has a negligible impact on the predicted noise. For low frequencies, the segmentation model yields converged results with a small number of segments; only at higher frequencies is $N = 20$ necessary to achieve convergence. Notably, for large N, the AR of the segments falls below the recommended threshold of 3; however, the predictions remain consistent for both LE and TE cases, suggesting the robustness of the segmentation approach even in this condition. The predictions obtained with the ring models are also shown as a preliminary comparison. While the difference between the two TE noise models is approximately 2 dB, larger differences are observed for the LE noise models, for which approximately 8 dB differences are observed. The comparison between the two approaches is further investigated in Secs. III B and III C.

It might be argued that, for a large number of segments or incident turbulence containing large eddies, the span length L of the segments becomes comparable with the turbulence correlation length λ and, hence, the noise emitted by adjacent segments is not fully uncorrelated. Formally, the condition is satisfied for $L/\lambda \gg 1$. For TE noise, the azimuthal correlation length l_y is considered as the characteristic length scale for the turbulent eddies λ. The stricter condition applies at low frequency for which $l_y(\omega, k_y)$ is the highest. At low frequency, we can suppose that the most important contributions are related to spanwise wavenumbers $k_y \approx 0$, and, hence, at, e.g., $f_0 = 100$ Hz, we obtain $\lambda = l_y(2\pi f_0, 0) \approx 0.08$ m. For the LE noise, the integral

length scale $\Lambda_f = 0.015$ m is used as the characteristic length scale of the turbulent eddies λ. Figure 4 shows that no significant differences are present between the PSD computed with $N = 6$ segments, corresponding to a span length of the segments of $L = 1$ m (i.e., $L/\lambda \gg 1$), and with $N = 100$ segments, for which $L = 0.063$ m is in the same order of magnitude of λ. From this consideration, it can be concluded that, even if the condition $L/\lambda \gg 1$ is not strictly satisfied, the effect on the results is negligible.

Based on the observed results, $N = 20$ was deemed an appropriate choice to balance the computational efficiency, prediction accuracy, and maintain a reasonable AR for the segments.

B. Leading-edge noise

Figure 5 presents the LE noise computed using the segmentation approach [Eq. (21)] and ring model [Eq. (15)]. The ring has a radius $r_0 = 0.05$ m and a chord $c = 0.03$ m. The observer positions are located at 30°, 60°, 90°, and 120° relative to the upstream direction, at a distance of 1.3 m ($26 \times r_0$) from the ring's center. The results are compared against experimental data, and the computations with the ring model of Roger (2010). In the measurements, the ring was placed in the shear layer of a jet with an exit flow speed of 38 m s^{-1}. As explained in Roger (2010), the average velocity at $r = r_0$ was $U = 23$ m s^{-1} ($M = 0.067$). This flow speed is used in the analytical model computations. We computed the inflow turbulence spectrum Φ_{ww} using the two-dimensional von Kármán turbulence spectrum model of Eq. (23), using $u_{rms} = 6.71$ m s^{-1} and $\Lambda_f = 1.5$ cm. Alternatively, Roger (2010) calculated the turbulence spectrum Φ_{ww} using a radial velocity spectrum with the associated azimuthal correlation length. Furthermore, Roger (2010) applied a correction to account for the anisotropy found in the mixing layer of the jet. The implementation of these corrections falls out of the scope of this work because they are specific to the application studied in Roger (2010) (i.e., jet-ring interaction noise).

The results presented in Fig. 5 show a good agreement between our ring model and the results presented in Roger (2010), supporting the validity of our approach. The deviation between our results and the reference is explained by the differences in the model's input, Φ_{ww}, resulting from the different method used by Roger (2010) to calculate the turbulence spectrum. The improved agreement of Roger (2010) with the experiment arises from the corrected input spectrum rather than from modifications to the ring model. In contrast, the segmentation model yields lower values, with an offset of 8 dB, corresponding to a S_{pp} magnitude approximately 6.3 times lower than that predicted by the ring model. This discrepancy may result from the fundamental difference between the two models: the segmentation model assumes uncorrelated contributions from each segment, whereas the ring model enforces azimuthal mode coherence over the entire annulus, accounting for cross-correlations between different locations. This difference becomes more important at low frequencies, where the dominant acoustic contributions arise from the lowest-order azimuthal modes

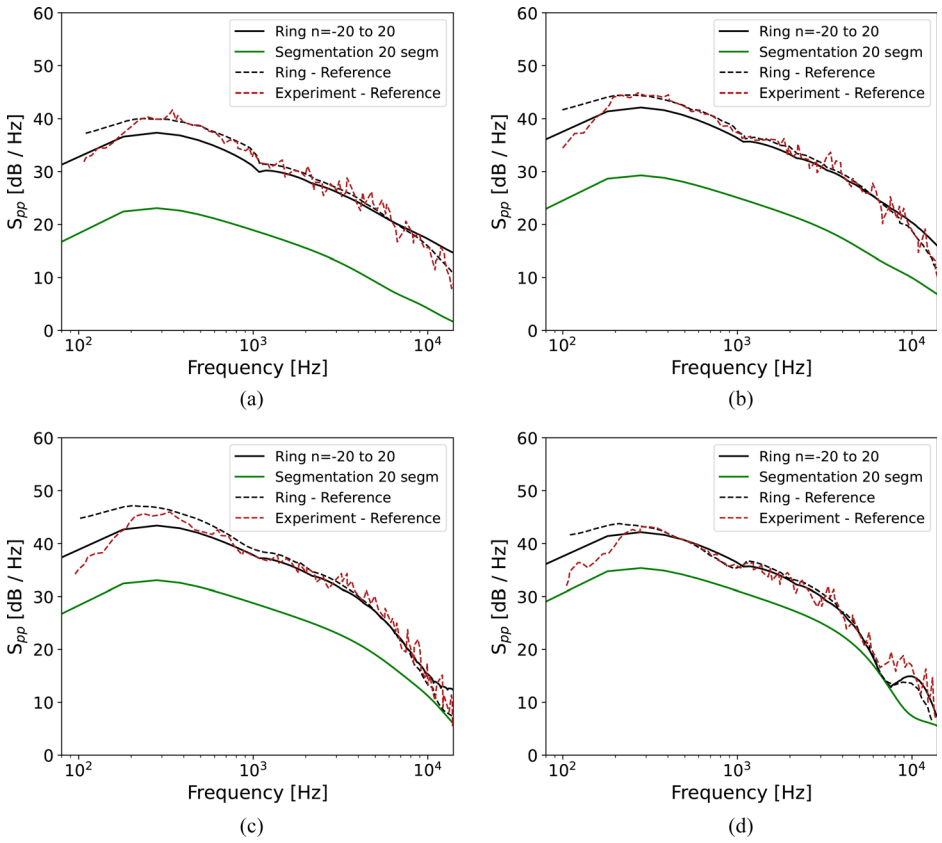

FIG. 5. Ring LE broadband noise PSD predictions at $R = 1.3$ m, compared with Ring model and experiment from Roger (2010), $M = 0.067$.

https://doi.org/10.1121/10.0039542

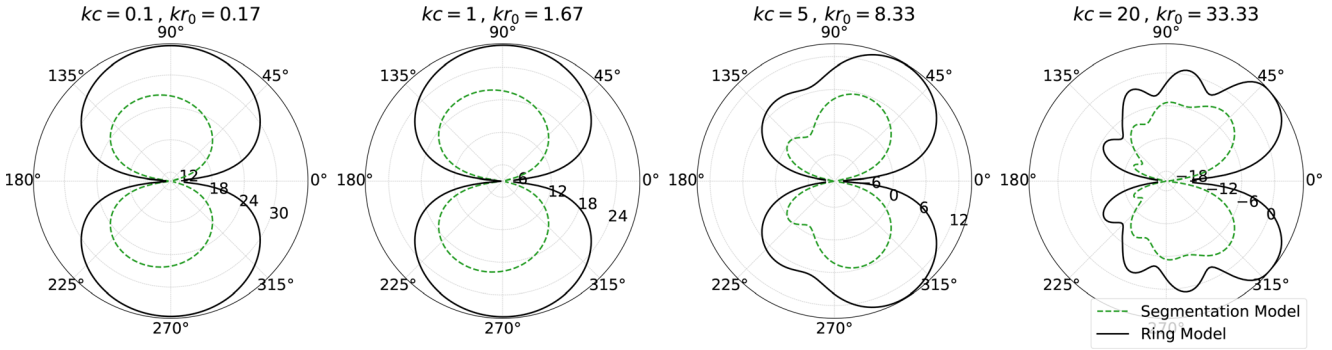

FIG. 6. LE noise directivity (S_{pp} dB Hz^{-1}) in the e_1e_2 plane with segmentation and annulus model at $kc = 0.1$, $kc = 1$, $kc = 5$, and $kc = 20$, and $kr_0 = (5/3)kc$. Flow direction: from left to right.

($n = 0$ and $n = \pm 1$), and where the assumption of uncorrelated segments is challenged due to larger turbulence structures interacting with multiple segments simultaneously.

Figure 6 shows a comparison of the ring's LE noise directivity using the ring model and the segmentation approach at $R = 3$ m, with reduced frequency $kc = 0.1$, $kc = 1$, $kc = 5$, and $kc = 20$ (and $kr_0 = (5/3)kc$). The comparison shows that the segmentation model underpredicts the ring model results at all shown frequencies. Regarding the directivity, at low reduced frequencies, we observe a symmetric dipolar radiation pattern. As the dimensionless frequency increases to $kc = 5$ and $kc = 20$, butterfly-shaped lobes appear. The mainlobe of the LE noise directivity is toward the TE, meaning that the LE noise is mainly radiated towards the downstream direction. Such behavior is anticipated, as it is also observed for an isolated airfoil at high kc [see, e.g., Roger and Moreau (2005)].

In terms of computational cost, both models require similar computation time when using a comparable number of modes and segments. In practice, the segmentation model typically converges with around 20 segments. However, to achieve higher accuracy at higher frequencies with the ring model, up to 100 modes may be required, making the ring approach more computationally demanding in those cases. Nonetheless, the ring model provides an exact solution for circular, thin geometries, whereas the segmentation model remains an approximation.

Figure 7 shows the contributions of individual azimuthal modes to the aeroacoustic transfer function, presented as directivity patterns at reduced frequencies, kc and kr_0. These contributions are normalized to c and r_0 and independent of observer distance and are expressed as $|kc\,\mathcal{L}^{LE}/S_0|\,|\mathcal{J}|$. For each reduced frequency, the directivity patterns of modes $n = 0$ to $n = \pm 3$ are shown and compared to the total sound field.

The directivity is symmetrical with a dipolar shape for low values of kc, regardless of the value of kr_0. This is explained by the fact that $\mathcal{L}^{LE}$ is independent of the ring's radius, and it is the only term of the normalized aeroacoustic transfer function that depends on the angular position of the observer. As expected from a physical point of view, only an increase in the wavenumber normalized by the chord kc is causing an asymmetry with respect to the upstream-downstream direction (e_2e_3 plane in Fig. 2). At the highest value of kc and kr_0, the maximum of the noise starts shifting toward the downstream direction, as shown in Fig. 10. This behavior is consistent with the explanation provided in Fig. 6 regarding the aeroacoustic transfer function and its dependence on kc. As kr_0 increases, the relative contribution of each mode becomes less pronounced, and a larger number of modes are required to capture the total sound field.

Figure 8 complements the information provided in Fig. 7 by showing the contributions from individual gust azimuthal modes n at the observer position of Fig. 5(a), 30°, $R = 26r_0$. The plot compares these contributions with the converged total noise computed. The contributions from individual modes demonstrate that the low and mid frequency ranges are mainly affected by the low-order modes ($n = 0$ and $n = \pm 1$). The remaining modes ($n < -1$ and $n > 1$) gain more importance in the high-frequency range, although none of them singularly dominate the total sound field.

Figure 9 shows the normalized aeroacoustic transfer function (same as in Fig. 7), expressed as $|kc\,\mathcal{L}^{LE}/S_0|\,|\mathcal{J}|$. For each combination of reduced frequencies kc and kr_0, different modes are progressively added to determine the number required for convergence. This is done by comparing the results with the converged solution, which includes modes ranging from $n = -200$ to $n = 200$. Initially, only the mode $n = 0$ is accounted for, followed by the sequential addition of modes $n = \pm 1$, $n = \pm 3$, $n = \pm 10$, and finally all modes between $n = \pm 20$ due to the increased significance of higher order terms in the Bessel function derivative $\mathcal{J}$. This behavior is independent of the chord length. From a physical point of view this can be explained by the fact that at high kr_0 the ring is not compact anymore in the azimuthal direction and, hence, the unsteady loading coming from higher azimuthal modes increasingly contributes to the overall sound field.

Figure 10 illustrates the LE thin annulus model computation at a distance of $R = 60\,r_0$ from the center of the ring, providing a three-dimensional view of the noise directivity at three different reduced frequencies: $kc = 1$, $kc = 5$, and $kc = 10$. The results reveal the expected axisymmetric directivity, verified across all three frequencies. As shown in Fig. 6, the frontal plane symmetry is only observed at lower

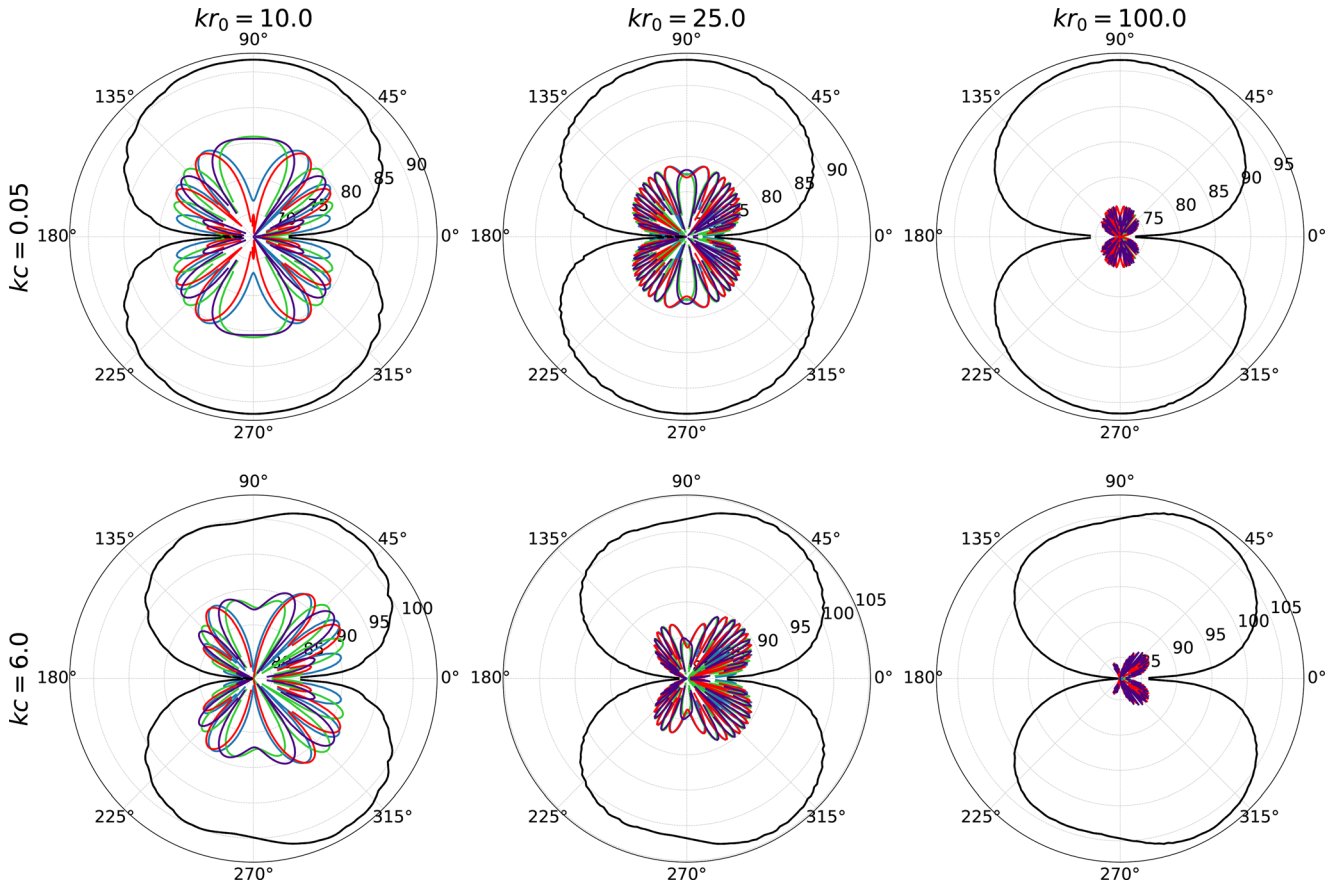

FIG. 7. Directivity patterns of the ring LE normalized aeroacoustic transfer function for individual azimuthal modes n in the meridional plane at reduced frequencies kr_0 ranging from 10 to 100 for $kc = 0.05$ and 6 and at $M = 0.1$. Flow direction: from left to right. Observer position: $(x_1, x_2, x_3) = (\cos\vartheta, 0, \sin\vartheta)$. Black line: Modes $n = -200$ to 200 (converged solution); blue line: Modes $n = 0$; green line: Modes $n = \pm 1$; red line: Modes $n = \pm 2$; purple line: Modes $n = \pm 3$.

reduced frequencies, while at higher frequencies a noticeable shift towards the TE occurs.

C. Trailing-edge noise

For the TE model, a ring geometry with $r = 1$ m and $c = 0.3$ m was used, to ensure applicability of the flat plate BL model. The inflow velocity of 30 m s^{-1} resulted in a chord-based Reynolds number $\mathrm{Re} = 0.6 \times 10^6$. Figure 11 presents the results for TE noise computed using the segmentation method [Eq. (22)] and ring model [Eq. (16)], and the observer positions are located $R = 26r_0$ at 30°, 60°, 90°, and 120°. Since there are no reference values or experimental data, only the analytical results calculated with the ring model and segmentation approach are shown. Overall, a better agreement than for the LE case is observed between the two approaches. Across all frequency ranges, the predictions of the ring model are consistently offset by approximately 2 dB compared to the segmentation approach, with the segmentation model under-predicting.

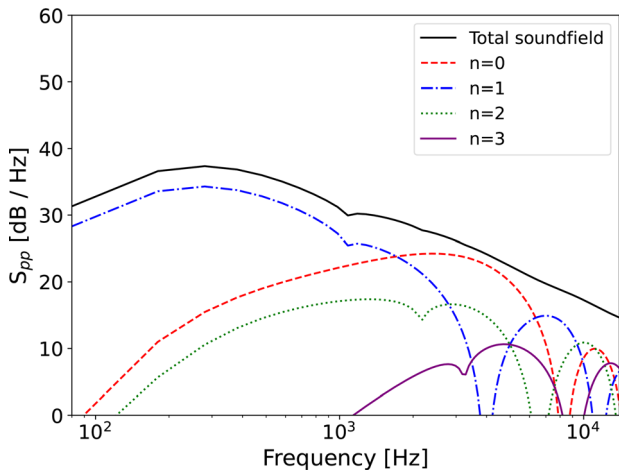

FIG. 8. Contribution of individual modes n to the total LE noise. Microphone at 30° and $R = 26\,r_0$.

The segmentation model is valid when the segment length is larger than the coherence length, which is satisfied in this study. This ensures that coherence issues do not explain the observed differences. Additionally, a convergence study in Sec. III A confirms the independence of the results from the number of segments used in the segmentation approach. Figure 12 compares the directivity of the TE PSD S_{pp}, using the ring model and the segmentation approach at $R = 26r_0$, with reduced frequencies $kc = 0.1$, $kc = 1$, $kc = 3$, and $kc = 10$ (and $kr_0 = (5/3)kc$). The results between the two models show differences below

https://doi.org/10.1121/10.0039542

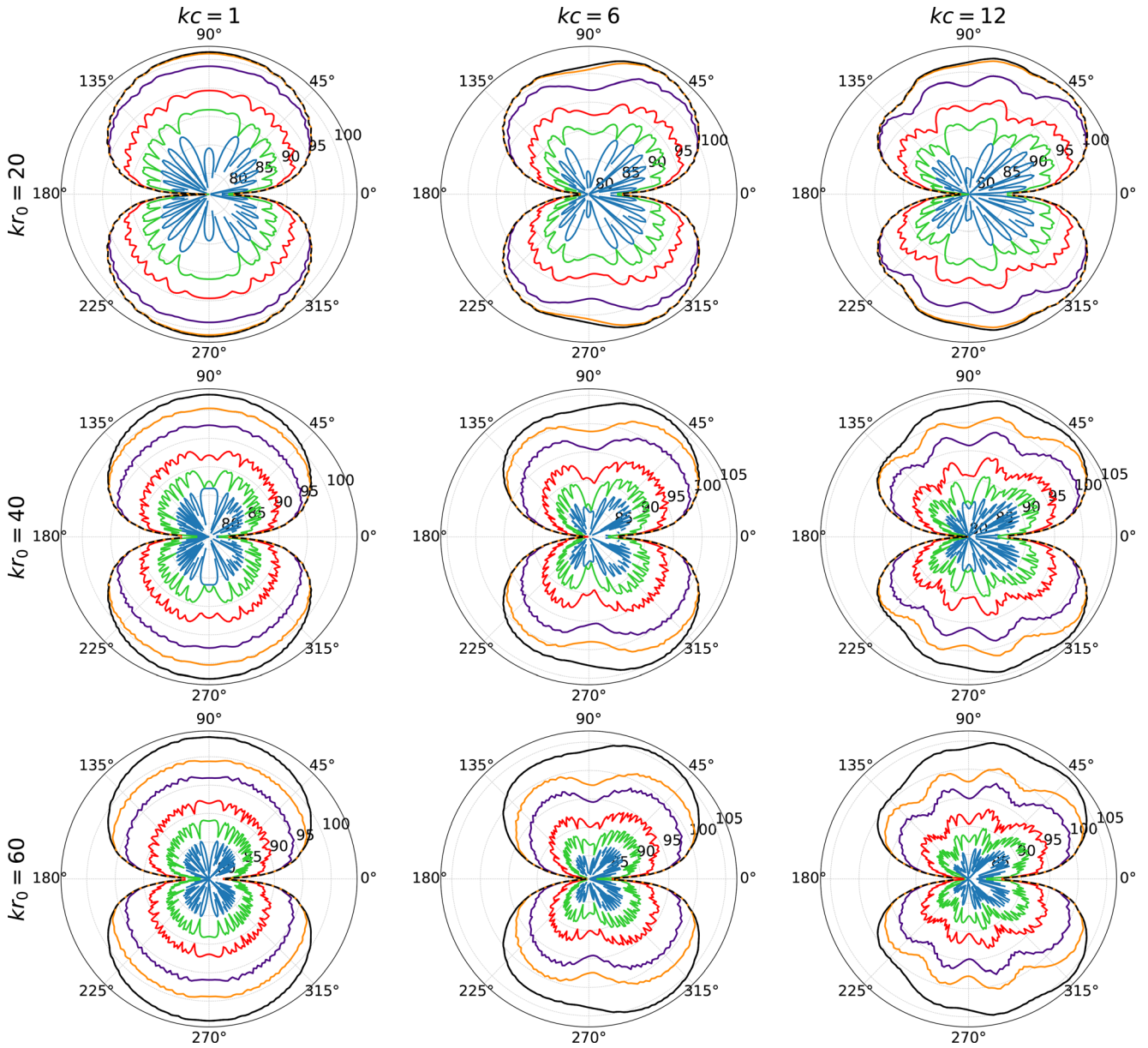

FIG. 9. Normalized aeroacoustic transfer function (LE) $|kc\,\mathcal{L}^{LE}/S_0|\,|\mathcal{J}|$ in the meridional plane with $M = 0.1$, at reduced frequencies $kc = 1$, $kc = 6$, $kc = 12$, and $kr_0 = 20$, $kr_0 = 40$, $kr_0 = 60$. Flow direction: from left to right. Observer position: $(x_1, x_2, x_3) = (\cos\vartheta, 0, \sin\vartheta)$. Black line: Modes $n = -200$ to 200 (converged solution); blue line: Modes $n = 0$; green line: Modes $n = -1$ to 1; red line: Modes $n = -3$ to 3; purple line: Modes $n = -10$ to 10; orange line: Modes $n = -20$ to 20.

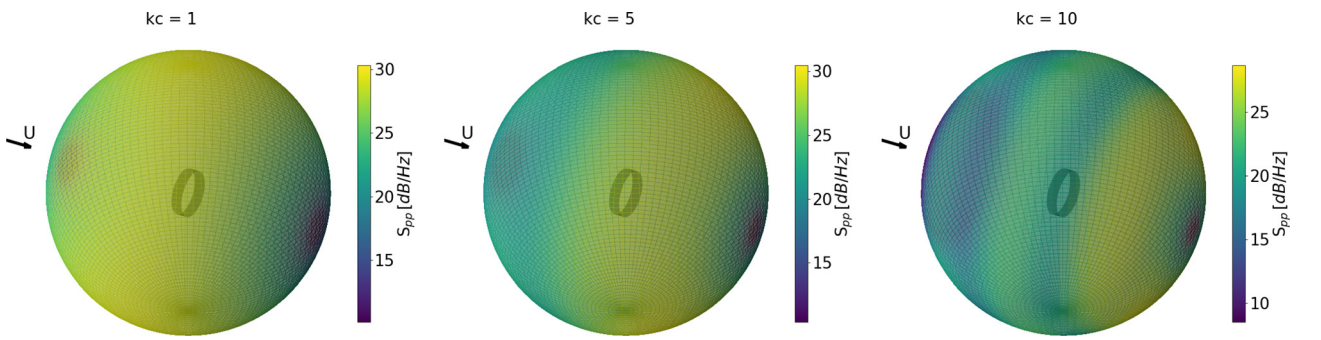

FIG. 10. Directivity of the PSD of LE noise represented on a sphere with radius centered on the ring, $R = 3$ m at reduced frequencies $kc = 1$, $kc = 5$, and $kc = 10$.

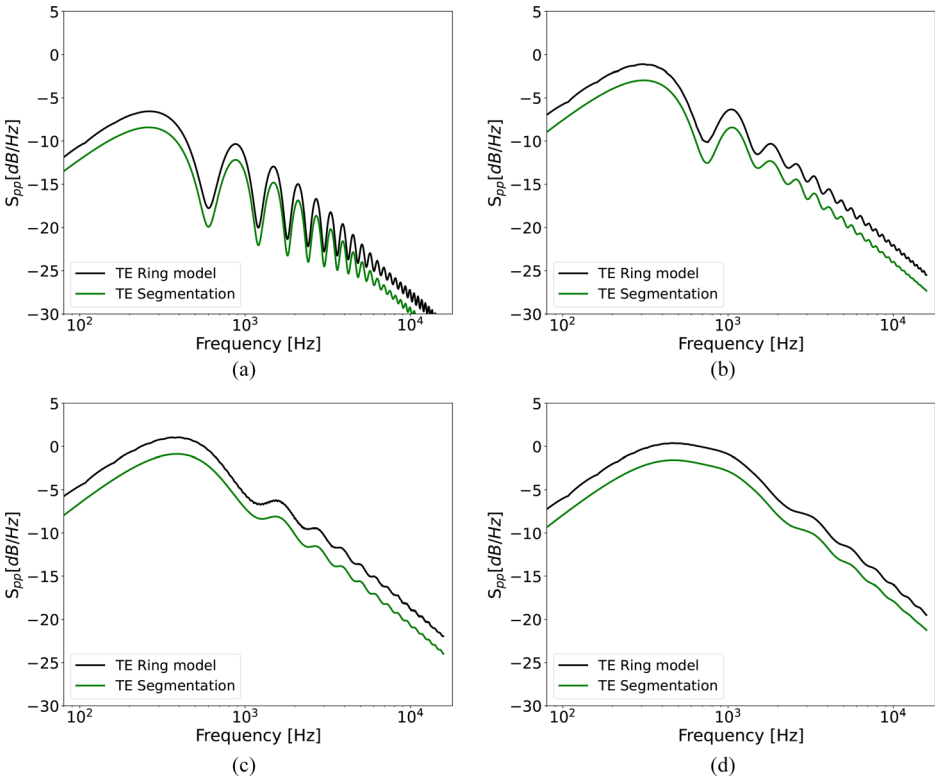

FIG. 11. Comparison of the TE PSD predictions at $R = 26\,r_0$ with the ring and segmentation models.

3 dB except for the lowest frequency. At the lowest frequency ($kc = 0.1$), we observe the largest discrepancy, with the segmentation model underpredicting by about 4 dB. At higher frequencies ($kc = 3$ and $kc = 10$), the segmentation model predicts the complex aeroacoustic transfer function directivity and lobes, despite overpredicting in certain directions.

Figure 13 shows the contributions of individual azimuthal modes, from $n = 0$ to $n = \pm 3$, to the normalized aeroacoustic transfer function, for various reduced frequencies kc and kr_0. These contributions, independent of the observer position, are normalized to c and r_0 and expressed as $|kc\,\mathcal{L}^{TE}/S_0|\,|\mathcal{J}|$. The expression for the normalized transfer function is very similar to the one in Fig. 9, differing only in that it uses $\mathcal{L}^{TE}$ instead of $\mathcal{L}^{LE}$. For that reason, we observe the same behaviors: lower-order modes are dominant for lower values of kr_0, repeating the results observed in the LE case.

Figure 14 presents the individual gust azimuthal mode n contribution to the TE PSD at the observer position of Fig. 11(a), i.e., 30°, $R = 26\,r_0$. The plot compares these contributions with the converged solution. The contributions from individual modes demonstrate how the dominant modes ($n = 0$ and $n = \pm 1$) shape the spectrum by affecting different frequency ranges. Because kc is higher in this case compared to the LE (Fig. 8), all modes, including the dominant modes ($n = 0$ and $n = \pm 1$), shift their contribution to lower reduced frequencies. For larger rings, it is crucial to include higher-order modes to ensure accurate predictions within the audible frequency range.

Figure 15 shows the ring's TE aeroacoustic transfer function, normalized to c and r_0, expressed as $|kc\,\mathcal{L}^{TE}/S_0|\,|\mathcal{J}|$.

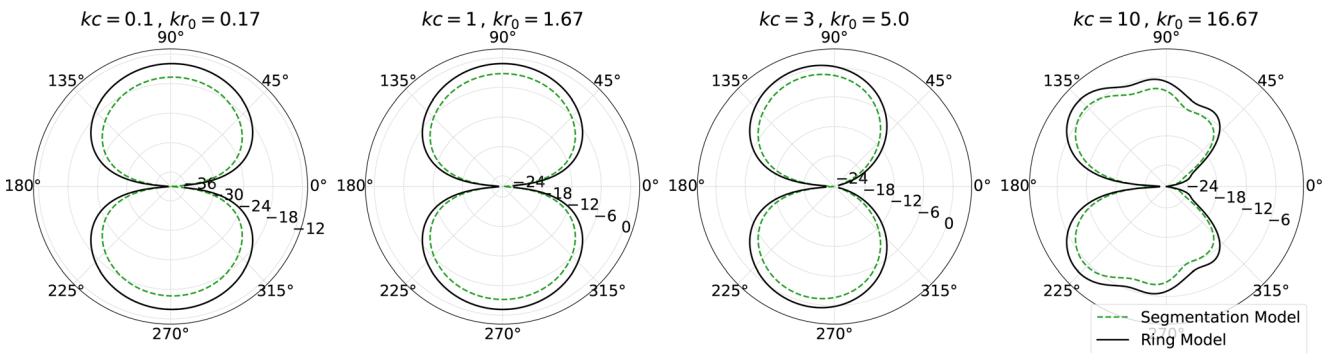

FIG. 12. TE noise directivity (S_{pp} dB Hz^{-1}) in the e_1e_2 plane with segmentation and annulus model at $kc = 0.1$, $kc = 1$, $kc = 3$, $kc = 10$, and $kr_0 = (5/3)kc$. Flow direction: from left to right.

https://doi.org/10.1121/10.0039542

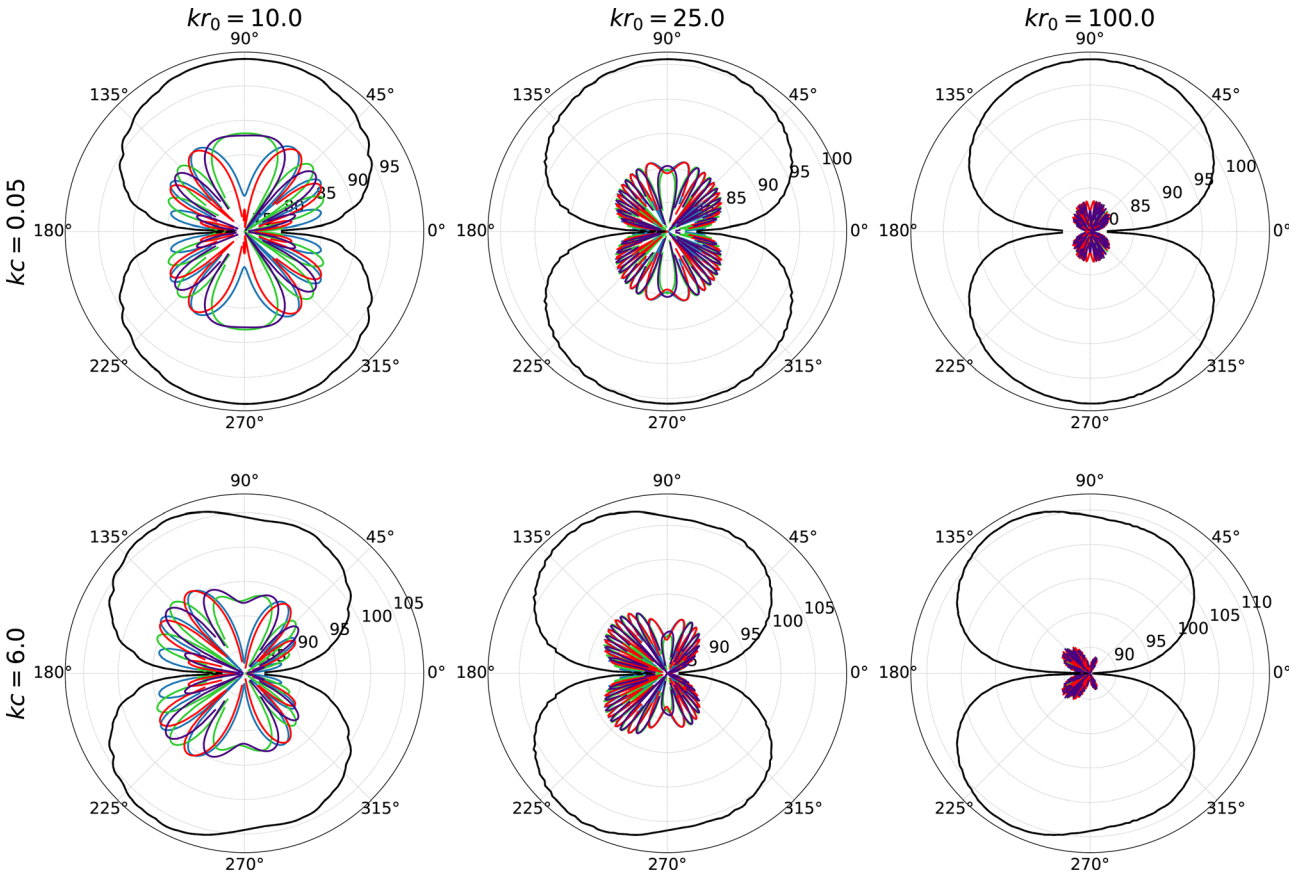

FIG. 13. Directivity patterns of the ring TE normalized aeroacoustic transfer function for individual azimuthal modes n in the meridional plane, at reduced frequencies kr_0 ranging from 10 to 100 for $kc = 0.05$ and 6 at $M = 0.1$. Flow direction: from left to right. Observer position: $(x_1, x_2, x_3) = (\cos\vartheta, 0, \sin\vartheta)$. Black line: Modes $n = -200$ to 200 (converged solution); blue line: Modes $n = 0$; green line: Modes $n = \pm 1$; red line: Modes $n = \pm 2$; purple line: Modes $n = \pm 3$.

For each combination of the reduced frequencies kc and kr_0, different modes are considered and compared with the converged solution. As observed in the LE case, the number of modes necessary to reach a converged solution increases with increasing kr_0. For example, accounting for the modes ranging from $n = -20$ to $n = 20$ is enough only at the lowest kr_0 shown in the figure ($kr_0 = 20$), while more modes are necessary to reach convergence at $kr_0 = 60$. Likewise, in the LE case, at low kc values, the directivity pattern remains symmetrical, reflecting dipole behavior regardless of kr_0. This is consistent with the aeroacoustic transfer function's independence from the ring's radius. At higher kc values, this symmetry breaks, and the highest magnitude shifts to the upstream direction, as observed previously.

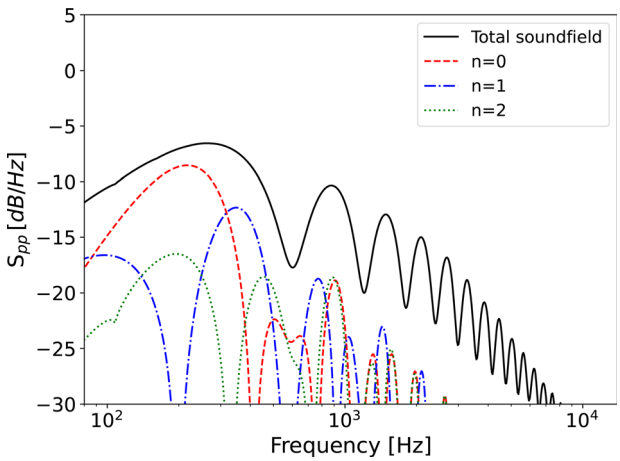

FIG. 14. Individual modes n relative contribution to TE S_{pp}, Microphone at 30° and $R = 26\,r_0$.

Figure 16 illustrates the TE thin annulus model computation at a distance $R = 60\,r_0$ from the center of the ring, providing a three-dimensional view of the noise directivity at three different reduced frequencies: $kc = 1$, $kc = 5$, and $kc = 10$. Similar to the LE case, we observe the expected axisymmetric directivity. However, for the TE noise, the intensity is more pronounced in the upstream direction. For low values of kc, the directivity patterns are symmetrical. For higher reduced frequency, the symmetry is broken and the highest magnitude shifts toward the upstream direction, explained by the directivity of the airfoil aeroacoustic transfer function $\mathcal{L}^{TE}$ (Bresciani *et al.*, 2022).

D. Effect of the flow conditions on the noise predictions

To evaluate how the ring model is impacted by the input parameters, a sensibility study was conducted on a ring with $r_0 = 1$ m and $c = 0.3$ m. Figure 17 shows the

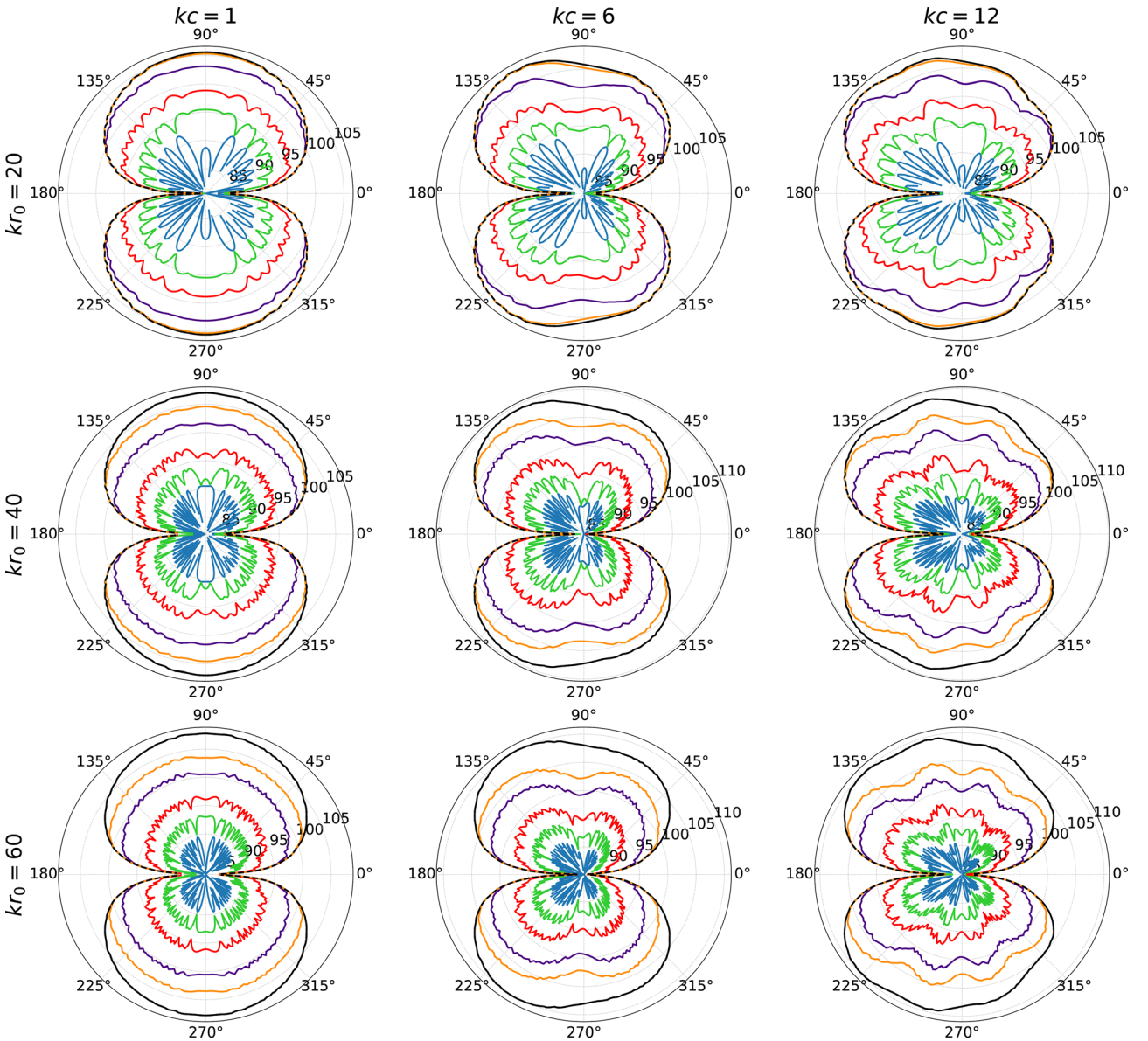

FIG. 15. Normalized aeroacoustic transfer function (TE) $|kc\,\mathcal{L}^{TE}/S_0|\,|\mathcal{J}|$ in the meridional plane with $M = 0.1$, at reduced frequencies $kc = 1$, $kc = 6$, $kc = 12$ and $kr_0 = 20$, $kr_0 = 40$, $kr_0 = 60$. Flow direction: from left to right. Observer position: $(x_1, x_2, x_3) = (\cos\vartheta, 0, \sin\vartheta)$. Black line: Modes $n = -200$ to 200 (converged solution); blue line: Modes $n = 0$; green line: Modes $n = -1$ to 1; red line: Modes $n = -3$ to 3; purple line: Modes $n = -10$ to 10; orange line: Modes $n = -20$ to 20.

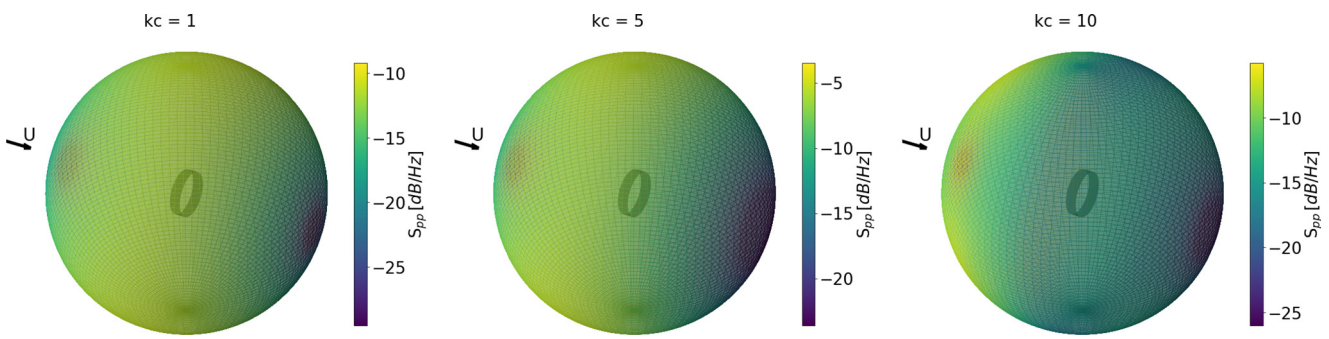

FIG. 16. TE S_{pp} directivity represented on a sphere centered on the ring, $R = 60\,r_0$ at reduced frequencies $kc = 1$, $kc = 5$, and $kc = 10$.

https://doi.org/10.1121/10.0039542

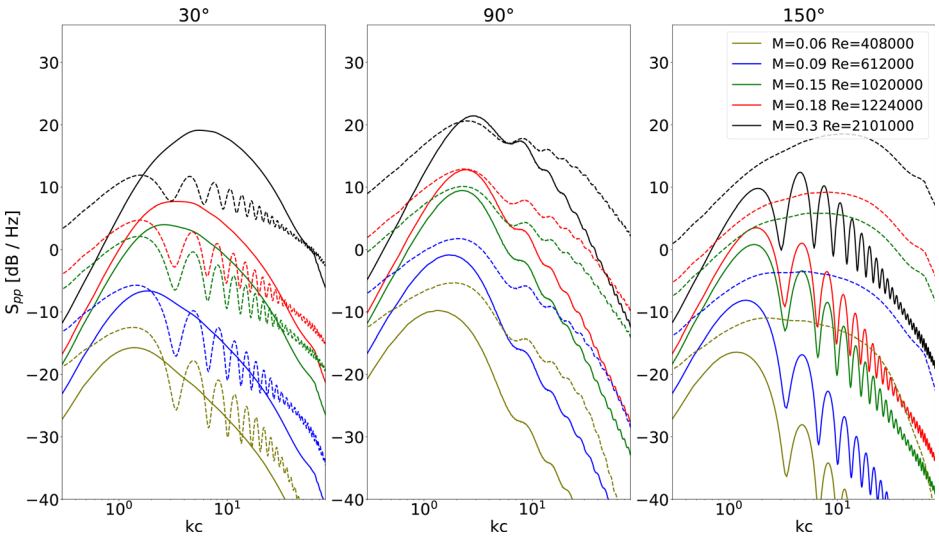

FIG. 17. LE (—) and TE (- -) PSD for different inflow velocities at observer distance $R = 26r_0$ and angular position 30° (upstream), 90°, and 150° (downstream).

effect of varying inflow velocity U with 0.1% turbulence intensity and a turbulence length scale of $\lambda_f = 0.015$ cm on both the LE and TE PSD at 30°, 90°, and 150° angular positions.

As expected, noise levels increase with Mach number for both the LE noise and TE noise. At 30°, for low Mach numbers, the LE and TE noise levels are nearly equivalent in this direction, but as velocity increases, LE noise scales more rapidly and becomes dominant under the prescribed turbulence conditions. At 90°, the LE noise and TE noise levels are of similar magnitude, with TE noise dominating both the low and high-frequency ranges, while LE noise becomes more significant in the mid-frequency range as the Mach number increases. In the downstream direction (150°), TE noise dominates across the entire frequency spectrum, with its peak shifting toward higher frequencies as the Mach number increases. The multiple interference peaks in the TE noise spectra for $kc \gg 1$ at 30° are indicative of non-compactness radiation effects. At 150°, a comparable multi-lobed spectrum shape is noticed in the PSD spectrum for LE noise, due to the mirrored nature of LE noise and TE noise directivities on the frontal (e_1, e_2) plane.

The effect of turbulence intensity on the LE noise enters as a multiplicative factor, as shown in Eq. (15), such that increasing the intensity raises the overall noise level without altering the spectral shape. In contrast, variations in the turbulence length scale modify the shape of the turbulence spectrum, which directly influences the predicted PSD. Moreover, larger turbulence scales increase spatial coherence across the annulus, which enhances correlations between segments and may amplify discrepancies with the ring model, particularly at low frequencies where large-scale structures dominate.

IV. CONCLUSIONS

This paper proposes two methods, based on Amiet's analytical theory, to predict LE and TE broadband noise generated by a circular geometry. The first method, referred to as the segmentation approach, discretizes the geometry as a set of flat plates. The noise emitted by the individual segments is modeled by the classical Amiet's theory and summed at the receiver position. In the second model, referred to as the thin annulus model, an analytical solution based on Amiet's theory is given for the special case of an infinitely thin circular annulus. Following the approach of Roger (2010), we extend the theory originally proposed for LE noise to the noise radiated by the TE of a thin annulus.

The thin annulus model predictions for LE noise agree with the experimental data and analytical results from Roger (2010), validating the implementation of the present work. In contrast, the segmentation model consistently underpredicts LE noise levels by approximately 8 dB. This difference is probably due to the missing cross correlation between adjacent segments, which is not considered in the segmentation model; however, due to the difficulty in quantifying this contribution, this remains the subject of future work. Regarding the TE noise, the segmentation model demonstrated good agreement with the thin annulus model, proving to be a viable option.

The thin annulus model has been used to analyze the contribution of the individual azimuthal mode to the total noise levels. The analysis revealed that modes $n = 0$ and $n = \pm 1$ define most of the low-frequency spectrum for both LE and TE noise, while higher modes contribute to the high-frequency range. A dependence was shown between the reduced frequency kr_0 and the number of modes n required for convergence. For rings with a large radius or at high frequency (high kr_0), high-order modes must be considered. Including modes from $n = -20$ to $n = 20$ ensured complete coverage up to $kr_0 = 20$. In the segmentation approach, using as few as 20 segments provided converged results. The computational cost of the thin annulus model is higher than the segmentation model at high kr_0 because of the high number of modes required by the thin annulus model to obtain a converged solution.

ACKNOWLEDGMENTS

This project has received funding from the European Union's Horizon 2020 research and innovation programme under the Marie Skłodowska-Curie Grant Agreement No. 860101.

AUTHOR DECLARATIONS

Conflict of Interest

The authors declare that they have no known competing financial interests or personal relationships that could have appeared to influence the work reported in this paper.

DATA AVAILABILITY

The data that support the findings of this study are available from the corresponding author upon reasonable request.

APPENDIX A: SEGMENTATION APPROACH

The segmentation approach requires a change of reference frame for every segment. This is because the observer's relative position **R** in a generic global reference frame x, y, z must be written in the segment j relative reference frame for all **N** segments. The global reference frame, schematized in Fig. 18 (left), has its origin centered with the ring.

The set of geometrical transformations executed to obtain the segment-observer relative position is described here. The first transformation is a rotation around the x axis, to adjust the alignment of the reference frame to any segment's respective θ angle. Such rotation is schematized in Fig. 18 (right). Then, as shown in Fig. 19 (left), a translation is applied to move the reference frame from the ring's center toward the center of the flat plate.

After that, the reference frame is placed following Amiet's theory: In the case of TE noise, the reference frame should be placed on the TE; In the case of LE noise, the reference frame must be placed at mid-chord.

The relative coordinates for each segment j are obtained using

$$\begin{aligned}\mathbf{x_{1j}} &= R_x - l,\\ \mathbf{x_{2j}} &= R_y\cos\theta_j - R_z\sin\theta_j,\\ \mathbf{x_{3j}} &= R_y\sin\theta_j + R_z\cos\theta_j - r_0,\end{aligned}$$

and

$$\mathbf{S_{0j}} = \sqrt{x_{1j}^2 + \beta^2(x_{2j}^2 + x_{3j}^2)} = \sqrt{(R_x - l)^2 + \beta^2\Big(\big(R_y\cos\theta_j - R_z\sin\theta_j\big)^2 + \big(R_y\sin\theta_j + R_z\cos\theta_j - r_0\big)^2\Big)}, \tag{A1}$$

with $l = 0$ for the LE or $l = c/2$ for the TE case.

APPENDIX B: AEROACOUSTIC TRANSFER FUNCTION OF THE RING MODEL

The linearized wave equation for the velocity potential, Φ, in cylindrical coordinates (r, θ, z) is given by

$$\nabla^2\Phi - \frac{1}{c_0^2}\frac{\mathrm{D}^2\Phi}{\mathrm{D}t^2} = 0, \tag{B1}$$

where ∇^2 is the Laplacian operator in cylindrical coordinates, c_0 is the speed of sound, Φ is the velocity potential, and $\mathrm{D}^2/\mathrm{D}t^2$ is the material derivative. Given the premise of longitudinal flow, the material derivative can be defined as

$$\frac{\mathrm{D}^2\Phi}{\mathrm{D}t^2} = \frac{\partial}{\partial t} + U\frac{\partial}{\partial z}. \tag{B2}$$

In cylindrical coordinates, the Laplacian ∇^2 of a scalar field $\Phi(r, \theta, z)$ is expressed as

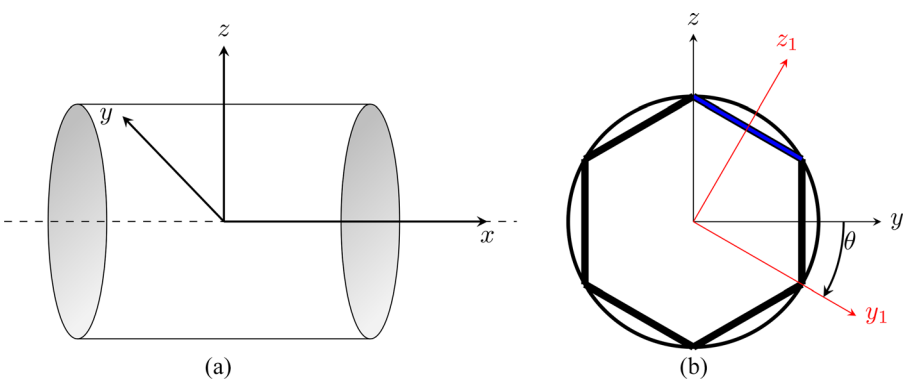

FIG. 18. Global reference frame (left) and transformation 1: θ rotation schematic (right).

https://doi.org/10.1121/10.0039542

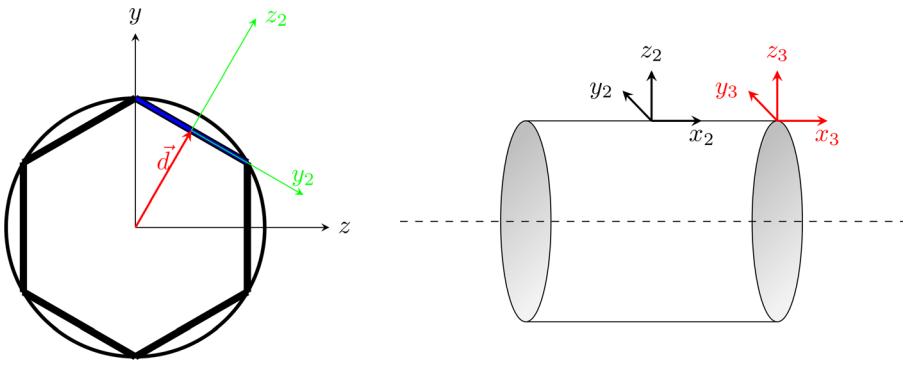

(a) (b)

FIG. 19. Transformation 2: translation to segments plane (left) and transformation 3: translation to TE (right).

$$\nabla^2\Phi = \underbrace{\frac{\partial^2\Phi}{\partial r^2} + \frac{1}{r}\frac{\partial\Phi}{\partial r}}_{\frac{1}{r\partial r}\left(r\frac{\partial\Phi}{\partial r}\right)} + \frac{1}{r^2}\frac{\partial^2\Phi}{\partial\theta^2} + \frac{\partial^2\Phi}{\partial z^2}. \tag{B3}$$

Substituting the Laplacian term into the wave equation [Eq. (B1)] yields

$$\frac{\partial^2\Phi}{\partial r^2} + \frac{1}{r}\frac{\partial\Phi}{\partial r} + \frac{1}{r^2}\frac{\partial^2\Phi}{\partial\theta^2} + \frac{\partial^2\Phi}{\partial z^2} - \frac{1}{c_0^2}\frac{\mathrm{D}^2\Phi}{\mathrm{D}t^2} = 0. \tag{B4}$$

This equation describes the evolution of the velocity potential Φ and consequently the velocity and pressure fields over time in a cylindrical coordinate system, taking into account the propagation of waves in a medium with cylindrical symmetry,

$$\frac{\partial^2\Phi}{\partial r^2} + \frac{1}{r}\frac{\partial\Phi}{\partial r} + \frac{1}{r^2}\frac{\partial^2\Phi}{\partial\theta^2} + \frac{\partial^2\Phi}{\partial z^2} - \frac{1}{c_0^2}\left[\frac{\partial^2\Phi}{\partial t^2} + 2U\frac{\partial^2\Phi}{\partial t\partial z} + U^2\frac{\partial^2\Phi}{\partial z^2}\right] = 0. \tag{B5}$$

Taking $\beta^2 = 1 - M^2$ and given the relationship $M = U/c_0$,

$$\underbrace{\beta^2\frac{\partial^2\Phi}{\partial z^2}}_{1} + \underbrace{\frac{\partial^2\Phi}{\partial r^2}}_{2} + \underbrace{\frac{1}{r}\frac{\partial\Phi}{\partial r}}_{3} + \underbrace{\frac{1}{r^2}\frac{\partial^2\Phi}{\partial\theta^2}}_{4} - \underbrace{\frac{1}{c_0^2}\frac{\partial^2\Phi}{\partial t^2}}_{5} - \underbrace{\frac{2U}{c_0^2}\frac{\partial^2\Phi}{\partial t\partial z}}_{6} = 0. \tag{B6}$$

The flow potential in said coordinate system can be written in the form

$$\Phi(r,\theta,z,t) = \phi(z,r)\mathrm{e}^{\mathrm{i}\omega t}\mathrm{e}^{\mathrm{i}\gamma z}\mathrm{e}^{\mathrm{i}\alpha r_0\theta}, \tag{B7}$$

with $\gamma = \dfrac{k_z M}{\beta^2}$ and $\alpha = -k_n$,

where $k_z = \omega/U$ is the streamwise aerodynamic wavenumber and $k_n = n/r_0$ is the spanwise or azimuthal wavenumber. Similarly, the incident velocity perturbation can be written as

$$w = w_0\mathrm{e}^{\mathrm{i}\omega t}\mathrm{e}^{-\mathrm{i}k_z z}\mathrm{e}^{-\mathrm{i}k_n r_0\theta}. \tag{B8}$$

The separate terms of the wave Eq. (B6) are developed using the flow potential definition of Eq. (B7). Accordingly, term 1 can be re-written as

$$\beta^2\frac{\partial^2\Phi}{\partial z^2} = \beta^2\frac{\partial}{\partial z}\left(\frac{\partial}{\partial z}(\phi\mathrm{e}^{\mathrm{i}\omega t}\mathrm{e}^{\mathrm{i}\gamma z}\mathrm{e}^{\mathrm{i}\alpha r_0\theta})\right) = \beta^2\left(\frac{\partial^2\phi}{\partial z^2} + 2\mathrm{i}\gamma\frac{\partial\phi}{\partial z} - \phi\gamma^2\right)\mathrm{e}^{\mathrm{i}\omega t}\mathrm{e}^{\mathrm{i}\gamma z}\mathrm{e}^{\mathrm{i}\alpha r_0\theta}. \tag{B9}$$

The term 2 gives

$$\frac{\partial^2\Phi}{\partial r^2} = \frac{\partial}{\partial r}\left(\frac{\partial}{\partial r}(\phi\mathrm{e}^{\mathrm{i}\omega t}\mathrm{e}^{\mathrm{i}\gamma z}\mathrm{e}^{\mathrm{i}\alpha r_0\theta})\right) = \left(\frac{\partial^2\phi}{\partial r^2}\right)\mathrm{e}^{\mathrm{i}\omega t}\mathrm{e}^{\mathrm{i}\gamma z}\mathrm{e}^{\mathrm{i}\alpha r_0\theta}. \tag{B10}$$

The term 3 gives

$$\frac{1}{r}\frac{\partial\Phi}{\partial r} = \frac{1}{r}\frac{\partial\phi}{\partial r}\mathrm{e}^{\mathrm{i}\omega t}\mathrm{e}^{\mathrm{i}\gamma z}\mathrm{e}^{\mathrm{i}\alpha r_0\theta}. \tag{B11}$$

The term 4 gives

$$\frac{1}{r^2}\frac{\partial^2\Phi}{\partial\theta^2} = \frac{1}{r^2}\phi\mathrm{e}^{\mathrm{i}\omega t}\mathrm{e}^{\mathrm{i}\gamma z}\frac{\partial^2}{\partial\theta^2}(\mathrm{e}^{\mathrm{i}\alpha r_0\theta}) = \frac{-\alpha^2 r_0^2}{r^2}\phi\mathrm{e}^{\mathrm{i}\omega t}\mathrm{e}^{\mathrm{i}\gamma z}\mathrm{e}^{\mathrm{i}\alpha r_0\theta}. \tag{B12}$$

The term 5 gives

$$-\frac{1}{c_0^2}\frac{\partial^2\Phi}{\partial t^2} = -\frac{1}{c_0^2}\phi\mathrm{e}^{\mathrm{i}\gamma z}\mathrm{e}^{\mathrm{i}\alpha r_0\theta}\frac{\partial^2}{\partial t^2}(\mathrm{e}^{\mathrm{i}\omega t}) = k^2\,\phi\mathrm{e}^{\mathrm{i}\omega t}\mathrm{e}^{\mathrm{i}\gamma z}\mathrm{e}^{\mathrm{i}\alpha r_0\theta}. \tag{B13}$$

Finally, the term 6 gives

$$-\frac{2U}{c_0^2}\frac{\partial^2\Phi}{\partial t\partial z} = -\frac{2U}{c_0^2}\frac{\partial}{\partial z}\left(\frac{\partial\Phi}{\partial t}\right) = \left(-\frac{2U}{c_0^2}\frac{\partial\phi}{\partial z}\mathrm{i}\omega + \frac{2U}{c_0^2}\,\phi\omega\gamma\right)\mathrm{e}^{\mathrm{i}\omega t}\mathrm{e}^{\mathrm{i}\gamma z}\mathrm{e}^{\mathrm{i}\alpha r_0\theta}. \tag{B14}$$

Joining the developed terms in (B6) leads to Eq. (B15):

$$\frac{\partial^2\phi}{\partial z^2}(\beta^2)+\frac{\partial\phi}{\partial z}\left(2\beta^2\mathrm{i}\gamma-\frac{2U}{c_0^2}\mathrm{i}\omega\right)+\phi\left(-\beta^2\gamma^2-\frac{\alpha^2 r_0^2}{r^2}+k^2+\frac{2U}{c_0^2}\omega\gamma\right)+\frac{\partial^2\phi}{\partial r^2}(1)+\frac{\partial\phi}{\partial r}\left(\frac{1}{r}\right)=0. \tag{B15}$$

Developing the $\partial\phi/\partial z$ term, we get

$$2\beta^2\mathrm{i}\gamma-\frac{2U}{c_0^2}\mathrm{i}\omega=2\mathrm{i}\left(\beta^2\gamma-\frac{U}{c_0}\frac{\omega}{c_0}\right)=k_zM-Mk_z=0.$$

The ϕ term can be simplified

$$\begin{aligned}&-\beta^2\gamma^2-\frac{\alpha^2 r_0^2}{r^2}+k^2+\frac{2U}{c_0^2}\omega\gamma\\&=-\frac{k^2M^2\beta^2}{\beta^4}+k^2+\frac{2U\omega\gamma}{c_0^2}-\frac{\alpha^2 r_0^2}{r^2}\\&=\frac{k^2}{\beta^2}-\frac{\alpha^2 r_0^2}{r^2}.\end{aligned}$$

We then obtain a simpler Eq. (B16),

$$\beta^2\frac{\partial^2\phi}{\partial z^2}+\frac{\partial^2\phi}{\partial r^2}+\left(\frac{1}{r}\right)\frac{\partial\phi}{\partial r}+\left(\frac{k^2}{\beta^2}-\frac{\alpha^2 r_0^2}{r^2}\right)\phi=0. \tag{B16}$$

Roger (2010) shows through a non-dimensional analysis that the term $(1/r)(\partial\phi/\partial r)$ may be discarded, providing the frequency is high enough for kh to be of order 1, h being the radial thickness of the annular fluid slice at $r=r_0$.

Upon dimensionalizing by the half chord b, we obtain

$$\bar{z}=\frac{z}{b},\quad \bar{r}=\frac{\beta r}{b},\quad \overline{\theta r}=\frac{\beta\theta r}{b}, \tag{B17}$$

$$\frac{\beta^2}{b^2}\frac{\partial^2\phi}{\partial\bar{z}^2}+\frac{\beta^2}{b^2}\frac{\partial^2\phi}{\partial\bar{r}^2}+\frac{\beta^2}{b^2}\frac{b^2}{\beta^2}\left(\frac{k^2}{\beta^2}-\frac{\alpha^2 r_0^2}{r^2}\right)\phi=0. \tag{B18}$$

Given the wave equation is analyzed in the annular section, the substitution $r=r_0$ leads to the simplification of the term ϕ,

$$\frac{\partial^2\phi}{\partial\bar{z}^2}+\frac{\partial^2\phi}{\partial\bar{r}^2}+\frac{b^2}{\beta^2}\left(\frac{k^2}{\beta^2}-\alpha^2\right)\phi=0. \tag{B19}$$

In the following canonical form, the expression obtained collapses to the Schwarzschild problem observed in the flat plate case, confirming the aeroacoustic transfer function is equivalent in both cases,

$$\frac{\partial^2\phi}{\partial\bar{z}^2}+\frac{\partial^2\phi}{\partial\bar{r}^2}+\kappa^2\phi=0, \tag{B20}$$

in which κ^2 is

$$\kappa^2=\frac{k^2b^2}{\beta^4}-\frac{b^2}{\beta^2}\alpha^2=\frac{\overline{k_z}^2M^2}{\beta^4}+\frac{\overline{k_n}}{\beta^2}.$$

This demonstrates that the value of κ^2 matches the solution obtained for the flat plate by Bresciani *et al.* (2022), indicating that the aeroacoustic transfer function is identical for the annulus case.

Ahmed, F., Zaman, I., Rezgui, D., and Azarpeyvand, M. (**2024**). "Aeroacoustics of a ducted fan ingesting an adverse pressure gradient boundary layer," J. Fluid Mech. **985**, R1-1–R1-13.

Amiet, R. K. (**1975**). "Acoustic radiation from an airfoil in a turbulent stream," J. Sound Vib. **41**(4), 407–420.

Amiet, R. K. (**1976**). "Noise due to turbulent flow past a trailing edge," J. Sound Vib. **47**(3), 387–393.

Blandeau, V. P., and Joseph, P. F. (**2011**). "Validity of Amiet's model for propeller trailing-edge noise," AIAA J. **49**, 1057–1066.

Botero-Bolívar, L., dos Santos, F. L., Venner, C. H., and de Santana, L. D. (**2023**). "Experimental and predicted leading- and trailing-edge noise of symmetric airfoils under zero mean-loading," Appl. Acoust. **212**, 109579.

Bresciani, A. P. (**2024**). "Physical and perceptual prediction of wind turbine noise," Ph.D. thesis, University of Twente, Enschede, The Netherlands.

Bresciani, A. P., Le Bras, S., and de Santana, L. D. (**2022**). "Generalization of Amiet's theory for small reduced-frequency and nearly-critical gusts," J. Sound Vib. **524**, 116742.

Bridges, J., Envia, E., and Huff, D. (**2001**). "Recent Developments in U.S. Engine Noise Reduction Research." Technical Memorandum No. 2001-211083 (NASA, Washington, DC).

Brooks, T., and Hodgson, T. (**1981**). "Trailing edge noise prediction from measured surface pressures," J. Sound Vib. **78**(1), 69–117.

Brooks, T. F., Pope, D. S., and Marcolini, M. A. (**1989**). "Airfoil Self-Noise and Prediction." NASA Reference Publication No. 1218 (NASA, Washington, DC).

Christophe, J., Anthoine, J., and Moreau, S. (**2009**). "Amiet's theory in spanwise-varying flow conditions," AIAA J. **47**, 788–790.

Cohen, E., and Gloerfelt, X. (**2018**). "Influence of pressure gradients on wall pressure beneath a turbulent boundary layer," J. Fluid Mech. **838**, 715–758.

Corcos, G. M. (**1964**). "The structure of the turbulent pressure field in boundary-layer flows," J. Fluid Mech. **18**, 353–378.

Devenport, W. J., Staubs, J. K., and Glegg, S. A. (**2010**). "Sound radiation from real airfoils in turbulence," J. Sound Vib. **329**(17), 3470–3483.

dos Santos, F. L., Botero-Bolívar, L., Venner, C. H., and de Santana, L. D. (**2023**). "Wall-pressure spectra, spanwise correlation, and far-field noise measurements of a NACA 0008 airfoil under uniform and turbulent inflows," Appl. Acoust. **211**, 109546.

Ffowcs Williams, J. E., and Hall, L. H. (**1970**). "Aerodynamic sound generation by turbulent flow in the vicinity of a scattering half plane," J. Fluid Mech. **40**(4), 657–670.

Freire-Guimaraes, J. M., Avallone, F., and Ragni, D. (**2022**). "Noise source identification on a diffuser-augmented wind turbine using Ffowcs Williams–Hawkings analogy," in *Book of Proceedings 18th EAWE PhD Seminar*, pp. 133–136, https://phd2022.eawe.eu/program/book-of-abstracts/.

Gonçalves, R. (**2025**). "Aerodynamics and aeroacoustics of diffuser-augmented wind turbines," Ph.D. thesis, University of Twente, Enschede, Netherlands.

Goody, M. (**2004**). "Empirical spectral model of surface pressure fluctuations," AIAA J. **42**(9), 1788–1794.

Griffin, K. P., Fu, L., and Moin, P. (**2021**). "General method for determining the boundary layer thickness in nonequilibrium flows," Phys. Rev. Fluids **6**, 024608.

Henderson, B., Kinzie, K., and Haskin, H. (**2004**). "The effect of nozzle trailing edge thickness on jet noise," in *Proceedings of the 10th AIAA/CEAS Aeroacoustics Conference*, Manchester, UK (May 10–12).

Howe, M. S. (**1978**). "A review of the theory of trailing edge noise," J. Sound Vib. **61**(3), 437–465.

Howe, M. S. (**1999**). "Trailing edge noise at low Mach numbers," J. Sound Vib. **225**(2), 211–238.

https://doi.org/10.1121/10.0039542

Hwang, Y., Bonness, W. K., and Hambric, S. A. (**2009**). "Comparison of semi-empirical models for turbulent boundary layer wall pressure spectra," J. Sound Vib. **319**(1–2), 199–217.
Kucukcoskun, K., Christophe, J., Schram, C., and Tournour, M. (**2013**). "Broadband scattering of the turbulence-interaction noise of a stationary airfoil: Experimental validation of a semi-analytical model," Int. J. Aeroacoust. **12**, 83–102.
Malgoezar, A. M., Vieira, A., Snellen, M., Simons, D. G., and Veldhuis, L. L. (**2019**). "Experimental characterization of noise radiation from a ducted propeller of an unmanned aerial vehicle," Int. J. Aeroacoust. **18**(4-5), 372–391.
Moreau, S., and Roger, M. (**2009**). "Back-scattering correction and further extensions of Amiet's trailing-edge noise model. Part II: Application," J. Sound Vib. **323**(1-2), 397–425.
Na, Y., and Moin, P. (**1998**). "The structure of wall-pressure fluctuations in turbulent boundary layers with adverse pressure gradient and separation," J. Fluid Mech. **377**, 347–373.
Olsen, W., Gutierrez, O., and Dorsch, R. (**1973**). "The effect of nozzle inlet shape, lip thickness, and exit shape and size on subsonic jet noise," in *Proceedings of the 11th Aerospace Sciences Meeting*, Washington, DC (January 10–12).
Olsen, W., and Karchmer, A. (**1976**). "Lip noise generated by flow separation from nozzle surfaces," in *Proceedings of the 14th Aerospace Sciences Meeting*, Washington, DC (January 26–28).
Pargal, S., Wu, H., Yuan, J., and Moreau, S. (**2022**). "Adverse-pressure-gradient turbulent boundary layer on convex wall," Phys. Fluids **34**(3), 035107.
Pirozzoli, S., and Bernardini, M. (**2010**). "Wall pressure fluctuations in transonic shock/boundary layer interaction," Procedia Eng. **6**, 303–311.
Prandtl, L. (**1925**). "Bericht über Untersuchungen zur ausgebildeten Turbulenz" ("Report on investigations into developed turbulence"), ZAMM J. Appl. Math. Mech. Z. Angew. Math. Mech. **5**(2), 136–139.
Roger, M. (**2010**). "On broadband jet–ring interaction noise and aerofoil turbulence-interaction noise predictions," J. Fluid Mech. **653**, 337–364.
Roger, M., and Moreau, S. (**2004**). "Broadband self noise from loaded fan blades," AIAA J. **42**, 536–544.
Roger, M., and Moreau, S. (**2005**). "Back-scattering correction and further extensions of Amiet's trailing-edge noise model. Part 1: Theory," J. Sound Vib. **286**(3), 477–506.
Roger, M., and Moreau, S. (**2010**). "Extensions and limitations of analytical airfoil broadband noise models," Int. J. Aeroacoust. **9**(3), 273–305.
Salze, E., Bailly, C., Marsden, O., Jondeau, E., and Juve, D. (**2014**). "An experimental characterisation of wall pressure wavevector-frequency spectra in the presence of pressure gradients," in *Proceedings of the 20th AIAA/CEAS Aeroacoustics Conference*, Atlanta, GA (June 16–20).
Schlinker, R., and Amiet, R. (**1981**). "Helicopter rotor trailing edge noise," in *Proceedings of the 7th Aeroacoustics Conference*, Palo Alto, CA (October 5–7).
Stalnov, O., Paruchuri, C., and Joseph, P. (**2015**). "Prediction of broadband trailing-edge noise based on Blake model and Amiet theory," in *Proceedings of the 21st AIAA/CEAS Aeroacoustics Conference*, Dallas, TX (June 22–26).
Tian, Y. (**2016**). "Modeling of wind turbine noise sources and propagation in the atmosphere," Ph.D. thesis, Université Paris Saclay, Orsay, France.
Tian, Y., and Cotté, B. (**2016**). "Wind turbine noise modeling based on Amiet's theory: Effects of wind shear and atmospheric turbulence," Acta Acust. united Ac. **102**(4), 626–639.
White, F. M. (**2009**). "Mcgraw-Hill series in mechanical engineering," in *Fluid Mechanics*, 6th ed. (McGraw-Hill, New York).
Williams, J. F., and Gordon, C. (**1965**). "Noise of highly turbulent jets at low exhaust speeds," AIAA J. **3**(4), 791–793.
Wu, W., and Piomelli, U. (**2018**). "Effects of surface roughness on a separating turbulent boundary layer," J. Fluid Mech. **841**, 552–580.